Notice

This is a non-peer reviewed preprint submitted to EarthArXiv. This manuscript has been submitted to Geophysical Journal International on 24-07-2022 with reference number GJI-22-0610 (Status: In Revision). Please check for the most recent version before referencing or citing since subsequent revised versions may differ in text and content.

Details

Role of fluid on earthquake occurrence: Example of the 2019 Ridgecrest and the 1997, 2009 and 2016 Central Apennines sequences

Author

Kariche, Jugurtha**;** USTHB, Dept. of Geophysics, FSTGAT, Algiers, Algeria, Institut de Physique du Globe, CNRS-UMR751**6**, EOST - Strasbourg, F-´ 67084, France.

Contact: jkariche@gmail.com

Or by twitter: https://twitter.com/JkaricheKariche

Role of fluid on earthquake occurrence: Example of the 2019 Ridgecrest and the 1997, 2009 and 2016 Central Apennines sequences

Jugurtha Kariche[1,2]

[1] USTHB, Laboratoire de Géophysique, FSTGAT, Algiers, Algeria.

[2] Institut Terre et Environnement de Strasbourg (ITES), CNRS-UMR7063.

[*]Corresponding author: Jugurtha Kariche (jkariche@gmail.com)

July 2022

SUMMARY

This paper focuses on the study of the temporal evolution of seismicity and the role of fluids during major earthquake sequences that occurred in the central Apennines and Southern Walker Lane belt-Eastern California Shear Zone over the last two decades: The 1997 Colfiorito sequence, the 2009 L'Aquila sequence, the 2016 Amatrice-Norcia sequence, and the 2019 Ridgecrest sequence. The availability of different high-quality seismic catalogs offers the opportunity to evaluate in detail the temporal evolution of the earthquake's size distribution (or b-value) and propose a physical explanation based on the effect of the fluid flow process in triggering seismicity. For all seismic sequences, the b-value time series show a gradual decrease from a few months to one year before mainshocks. The gradual decrease in the b-value is interpreted in terms of coupled fluid-stress intensity as a gradual increase in earthquake activity due essentially to the short-term to intermediate-term pore-fluid fluctuations. For the 2016 Amatrice-Norcia sequence and the 2019 Ridgecrest sequence, the temporal variation of the b-value during the foreshock sequence is characterized by a double b-value minimum separated by a short-lived b-value increase as observed in laboratory experiments on water-saturated rocks. Based on laboratory experiment results, the observed short–term fluctuation of the b-value is presented here as an accelerating crack growth due essentially to the fluid flow instability. Despite that the occurrence of seismic precursors could have been predictable in areas with high dense seismic networks, the different b-value time series show difficulty to establish a correspondence between the duration of the foreshock activity and the magnitude of the next largest expected earthquake. This may suggest that the spatial and temporal evolution of fluid migration controls the size of the ruptures.

INTRODUCTION

Several studies have suggested a relation between the occurrence of earthquake sequences and the temporal change in the relative size distribution of earthquakes quantified by the Gutenberg-Richter (GR) b-value (Berg, 1968; Scholz, 1968; Smith, 1981; Wiemer & Wyss, 2000…). The analyzes of a series of 60 foreshocks and 428 aftershocks related to three moderate earthquakes occurred on the Fairbank region of Alaska shows that the Gutenberg-Richter (GR) b-value was abnormally low (between 0.34 to 0.45) before large events and was restored taking a typical value of 0.85 to 0.95 during and after each mainshocks (Berg, 1968). The seismicity analysis of the 1967 Caracas (Mw 6.7) earthquake sequence, the 1971 San Fernando (Mw 6.4) earthquake sequence, and the 1968-1978 New Zealand earthquake sequence reveal that the temporal variation in the b-value was remarkably coupled with the size of moderate to strong earthquakes. A large time scale decrease in the b-value associated with an acceleration of aseismic slip is observed before the Mw 8.1 Iquique, Chile and the Mw 9.0 Tohoku-Oki earthquakes (Nanjo et al., 2012; Scholz, 2019). Several studies argues that the acceleration of aseismic slip is favored by a variation of pore fluid pressure at depth (Segall & Rice, 1995; Ruhl et al., 2016;Cappa et al., 2019 ; De Barros et al., 2020). The gradual decrease in the b-value on a much shorter time scale is also observed in the four-month-long foreshock sequence preceding the 2009 L'Aquila earthquake (Gulia et al., 2016). The temporal variation of the b-value before L'Aquila mainshock correlate with the change of Vp/Vs from January to the April 6 (Lucente et al., 2010). The simulateous change in b-value and Vp/Vs in the case of the L'Aquila sequence may interpret as a nucleation process due to an overpressurised volume controlled by fluid migration at depth (Chiaraluce, 2012).

The comparison between the temporal evolution of b-value and the effective normal stress in California show a decrease in the b-value associated with a decrease in effective normal stressing rate (Khoshmanesh & Shirzaei.,2018). The maximum increase in the Coulomb stress rate (up to 0.45 bar/yr spanning the period from 2003 to 2010) along the central part of the San Andreas Fault system also coincides with the decrease in effective normal stress caused by the evolution of pore-fluid pressure at depth (Khoshmanesh & Shirzaei.,2018). These results argue that a strong correlation exists between the fluid migration and the temporal evolution of the b-value along the central part of the San Andreas fault. In the Southern Walker Lane belt (SWL)-Eastern California Shear Zone (ECSZ), high-resolution optical satellite imagery analysis reveals a considerable contribution of the inelastic processes to the total diffuse deformation following the 2019 Ridgecrest earthquake sequence (Antoine et al., 2021). The high Vp/Vs ratio covering the complex fault zones of the 2019 Ridgecrest foreshock-mainshock sequence (Tong et al., 2021) denotes that the change in the pore-fluid pressure near the Ridgecrest fault zone may be considered as one of the plausible mechanisms explaining the diffuse inelastic deformation observed during the 2019 Ridgecrest sequence. A stress changes modeling results taking onto account the variation in the Vp/Vs ratio due to the diffusive effect of fluids during the Mw6.4 Ridgecrest foreshock reveals that the value of fluid diffusivity necessary to trigger the next Mw7.1 mainshock is estimated to $\leq 2.32\ 10^4\ cm^2/s$ (Kariche, 2022). This value seems to be low compared with the value obtained by Hudnut et al., (1989) for the 1987 Superstition Hills sequence and may explain the difference in the time delay between mainshocks in relation with to the two sequences.

A laboratory fracturing experiment on fluid-saturated rocks also predicts a variation in the Vp/Vs due to the change in the rheological properties of the seismogenic crust following large earthquakes. Fracture mechanics modeling and laboratory experiments for dry and water-saturated specimens shows that the gradual decrease in the b-value related to a progressive increase in acoustic emission rate (AE) is only visible in water-saturated rocks (Main et al. 1990). Laboratory experiments at constant pore-fluid volume predict a fluctuation in the b-value before major cracks and argue the idea that the fluid affects considerably the size and the distribution of future cracks (Sammonds et al., 1992). Other strong correlations between b-value and fluid migration are also found in a crustal range of the Taiwan orogenic belt (Chen et al., 2019).

In this paper, I explore the influence of fluids migration on earthquake occurrence by analyzing the temporal evolution of seismicity for two tectonically active zones with available high-quality dense seismic networks: the Central Apennine (Italy) and the SWL-ECSZ. Several major seismic sequences are studied in details: the 1997 Colfiorito, the 2009 l'Aquila and the 2016 Amatrice-Norcia for the Central Apennine seismic zone and the 2019 Ridgecrest (CA) sequence for the SWL-ECSZ. These sequences are explored in terms of seismic productivity and related fluid migration. By analyzing the evolution of seismicity and stress redistribution, I found a causative relation between the pore fluid effect and the Spatio-temporal evolution of crack growth before and during major earthquakes. The results are also compared to the laboratory experiments for a better constrain of the role of fluids in the different phases of the earthquake generation.

METHODOLOGY

1. G-R b-value time series modeling

A first empirical relation between the frequencies and magnitudes of earthquakes is proposed by Gutenberg & Richter (1950):

$$Log_{10}[N(M)] = a - bM \qquad (1)$$

Where a and b are the G-R constants, M is the magnitude, and $N(M)$ is the number of earthquakes in a specific time window of events with a magnitude range between M and $\pm \delta M$.

The b-value for an entire catalog is estimated by the maximum likelihood value (Aki, 1965):

$$b = \frac{1}{ln(10)(\bar{M} - M_c)} \qquad (2)$$

Where $\overline{M}$ represents an average magnitude value for a population of earthquakes satisfying the condition $M \geq M_c$, and M_c is the magnitude of completeness defined as the lowest magnitude at which all the events in a space-time volume are detected (Wiemer & Wyss, 2000; Woessner & Wiemer, 2005).

The b-value time series can be rewritten as (Woessner & Wiemer, 2005):

$$b = \frac{Log_{10}(e)}{\left[\langle M\rangle - \left(M_c - {}^{\Delta M_{bin}}/_{2}\right)\right]} \qquad (3)$$

Where $\langle M \rangle$ represents the mean magnitude of the sample and ΔM_{bin} is the binning width of the catalogue (Aki, 1965).

The standard deviation of b-value can be obtained using the Shi & Bolt (1982) approach:

$$\delta b = 2.3\, b^2 \sqrt{\frac{\sum_i (M_i\ \{M\})}{n\ (n-1)}}$$

Where *n* is the sample size.

In order to evaluate the temporal variation of crack distribution on a seismogenic volume, the temporal variation in b-value is computed using the 3D frequency–magnitude approach of Wyss *et al.* (1998) with an appropriate time window. The b-value time series computation procedure used in this study and based on the fixed number of events technics is in general similar to those used by Gulia & Wiemer, (2019) or Dascher-Cousineau et al., (2020) which take into account the space-time evolution of Mc in the b-value estimation. The determination of Mc is based on the assumption that the seismic events are self-similar (Wiemer & Wyss, 2000). The most robust way to deal with the dependence of the b-value time series on Mc is to choose a large value of Mc for the entire time series catalog, but this approach led to maximizing uncertainties when the computation of the b-value is made for a smaller number of earthquakes sample.

The correct assessment of the completeness magnitude Mc for each earthquake sample used here is made according to the automatic correction of the completeness level of Mc through time using the Maximum curvature method (MAXC) (Wiemer & Wyss, 2000). The Mc and the b-value are performed simultaneously by computing the maximum value of the first derivate of the frequency-magnitude plot. The MAXC technique provides a reasonable resolution of the b-value over time and tends to minimize uncertainties due to smaller sample sizes compared with the b-value estimates using fixed Mc-approaches. In order to completely leave the underestimation of the Mc value over time, a value of 0.2-to 0.5 is added to the Mc-values by taking into account the fact that the overall shape of the time series is invariant for at least Mc ranges associated with each earthquake sequence.

For the 2019 Ridgecrest sequence, I use the highest confidence QTM seismicity catalog for Southern California (Ross *et al*. 2019)spanning the period from 2000 to 2018 and the USGS-NEIC updated high-resolution catalog for the period between March 2018 to March 2020 combined with the Shelly (2020) higher-resolution Ridgecrest datasets. For 1997, 2009, and 2016 Central Apennine sequences, I use the entire seismic catalog of the Istituto Nazionale Di Geofisica E Vulcanology covering the period between 1985 and 2018 combined with the catalog for the same region published by Gasperini *et al.* (2013) augmented by the recent high-resolution catalog of Tan et al. (2021) in relation with the 2016-2017 Amatrice-Norcia sequence.

2. Fluid flow and the evolution of seismicity

Taking into account the complexity of the earthquake generation, a realistic representation of the temporal evolution of seismicity following a seismic event can be expressed as (Utsu 1969; Utsu & Ogata 1995):

$$\frac{dN(t)}{dt} \propto \frac{k}{(c+t)^p} \qquad (4)$$

Where $\frac{dN(t)}{dt}$ represents the aftershock frequency, *t* is the time from the main shock triggered event, *k* is the productivity of aftershocks that depends on the total number of events, *p* is the power law exponent and *c* define the time delay before the onset of the power-law aftershock decay rate and depends on the rate of activity in the earlier part of the seismic sequence. The value of c is also related to the incompleteness of seismic catalogs after strong earthquakes. Guo & Ogata (1997) obtained a ranges of c values between 0.003d and 0.3d for various earthquake datasets. In our simulation, the c value is fixed as 0.01d. This value of c is selected to be the lowest possible in order to obtain sufficient aftershocks productivity in the very early part of the aftershock sequence (Enescu et al., 2007; Kariche et al., 2018).

Based on the Nur and Booker (1972) hypothesis, the aftershock frequency within a seismogenic volume can be proportional to the temporal evolution of pore-fluid pressure as:

$$\frac{dN}{dt} = \frac{1}{\alpha} \int \frac{\partial P}{\partial t}\, dv \qquad (5)$$

Where α is a constant that defines the pore-fluid pressure increase with a cracks evolution in appropriate volume v. *P* represents the pore-fluid pressure variation following an earthquake.

Taking into account the boundary conditions for a steady state source and if we suppose a linear fluid-flow process, a simple poroleastic solution is given by Malagnini *et al*. (2012):

$$P(x,t) = (P_0 - P_1) erfc\left(\frac{x}{2\sqrt{ct}}\right) + P_1 \quad (6)$$

Where *c* represents the value of fluid diffusivity and *erfc* is the complementary error function. For nucleation assisted by fluids, Abramowitz & Stegun (1970) wrote the *erfc* function as:

$$erfc\left(\frac{x}{2\sqrt{ct}}\right) = \frac{2}{\sqrt{\pi}} \int_{\frac{x}{2\sqrt{ct}}}^{\infty} e^{-\xi^2}\, d\xi \quad (7)$$

In this case, the initial and boundary conditions may be posed as:

$$\begin{cases} P(x=0, t>0) = P_0 = \lambda_f\, \rho_r\, gz \\ P(x>0, t=0) = P_1 = \rho_w gz \end{cases}$$

Where ρ_r and ρ_w are respectively the rocks and fluid density, λ_f is the pore fluid pressure coefficient for an arbitrary depth and range between 0.6 and 0.8 for fault reactivation assisted by fluid (Rikitake 1972).

Replacing the 1 D pore fluid pressure form on the Nur & Booker (1972) equation with choosing the complementary error as expressed by Abramowitz & Stegun (1970), a complete aftershocks pore-fluid diffusion solution may be written as:

$$\frac{dN}{dt} = \frac{1}{\alpha} \frac{(P_0 - P_1)}{2\sqrt{\pi c t^3}} \int_0^{\infty} x\, e^{\left(-\frac{x^2}{4ct}\right)}\, dx = \frac{(P_0 - P_1)\sqrt{c}}{\alpha\sqrt{\pi}} \frac{1}{\sqrt{t}} \quad (8)$$

This equation shows that in the presence fluid, the aftershocks decay is proportional to $\frac{1}{\sqrt{t}}$. However, if an external source does not provide a sufficient fluid volume, the transient signal will decrease and a permanent Omori type signal (1/t) will appear.

THE CENTRAL APENNINE SEQUENCE

The 1997, 2009 and 2016 Central Apennine earthquake sequences start with the 1997 Colfiorito (Umbria-Marche) sequence which struck the northern part of the Appenine in Italy

(Amato et al., 1998; Stramondo et al., 1999; Deschamps et al., 2000; Chiaraluce et al., 2003…). The Colfiorito sequence is characterized by six earthquakes with magnitude larger than 5.0 and two earthquakes with magnitude larger than 5.7 (Figure 1, Figure 2A & S2). The first earthquake occurred on September 26 at 00:33 UTC with a magnitude Mw =5.7. Nine hours later, another strong earthquake with Mw 6.0 struck the Colfiorito region with a 3 km distance from the first event (Amato et al., 1998). The Mw 5.7 event is considered as a foreshock preceding the Mw 6.0 mainshock (Amato et al., 1998). The hypocentral depth for the two events is approximatively equal and situated around 4 to 5 km depth (Figure 1, Figure 2A & Figure S2). The third event with a magnitude Mw =5.9 triggers 18 days after at 12 km south east of the first event (Figure S2). The analysis of the spatial and temporal evolution of seismicity related to the 1997 Colfiorito shows that the seismicity is mainly controlled by the poroelastic properties of the seismogenic zone and fluid low (Antonioli *et al.* 2005). Using the fluid triggering hypothesis, the value of fluid diffusivity able to trigger a 1997 Colfiorito sequence range is estimated between 2.2 x 10^5 and 9.0 x 10^5 cm^2/s (Antonioli *et al.* 2005).

On April 6, 2009 at 01h32 GMT, a devastating earthquake with a magnitude Mw 6.3 occurred on normal fault at intramontane basin near the city of L'Aquila (Figure 1). This sequence began with a series of foreshocks six months prior the mainshock in a ~4 km long band on the L'Aquila fault zone (Figure 2B; Figure S3). The near field seismic wave analysis shows that the Spatio-temporal evolution of foreshocks correlates with a clear variation in seismic wave properties at depth (Lucente *et al.* (2010). The Vp/Vs value rose from 1.85 to more than 1.92 near the epicenter area of the 2009 L'Aquila earthquake a week before the mainshock and decreased down to 1.85 a few hours before (Lucente *et al.*, 2010). According to the dilatancy-diffusion hypothesis (Nur, 1972; Scholz et al., 1973), the change in Vp/Vs near L'Aquila is interpreted as the variation in elastic properties of the medium due to the fluid migration along the L'Aquila fault zone (Lucente *et al.*, 2010; Chiaraluce, 2012; Scholz, 2019).

Based on the temporal change in the Vp/Vs ratio, the triggering mechanism related to the L'Aquila earthquake is resolved as a mechanism governed by the presence of a deep large fluid reservoir (Lucente et al. 2010). Indeed, the complexity of the fault zone, the deep thrust fault, and the low angle active normal faults observed nearby the L'Aquila major rupture (Chiodini et al., 2004) may be interpreted as a structural seal that favors the fluid accumulation and creates an overpressurized volume near the L'Aquila hypocentral depth.

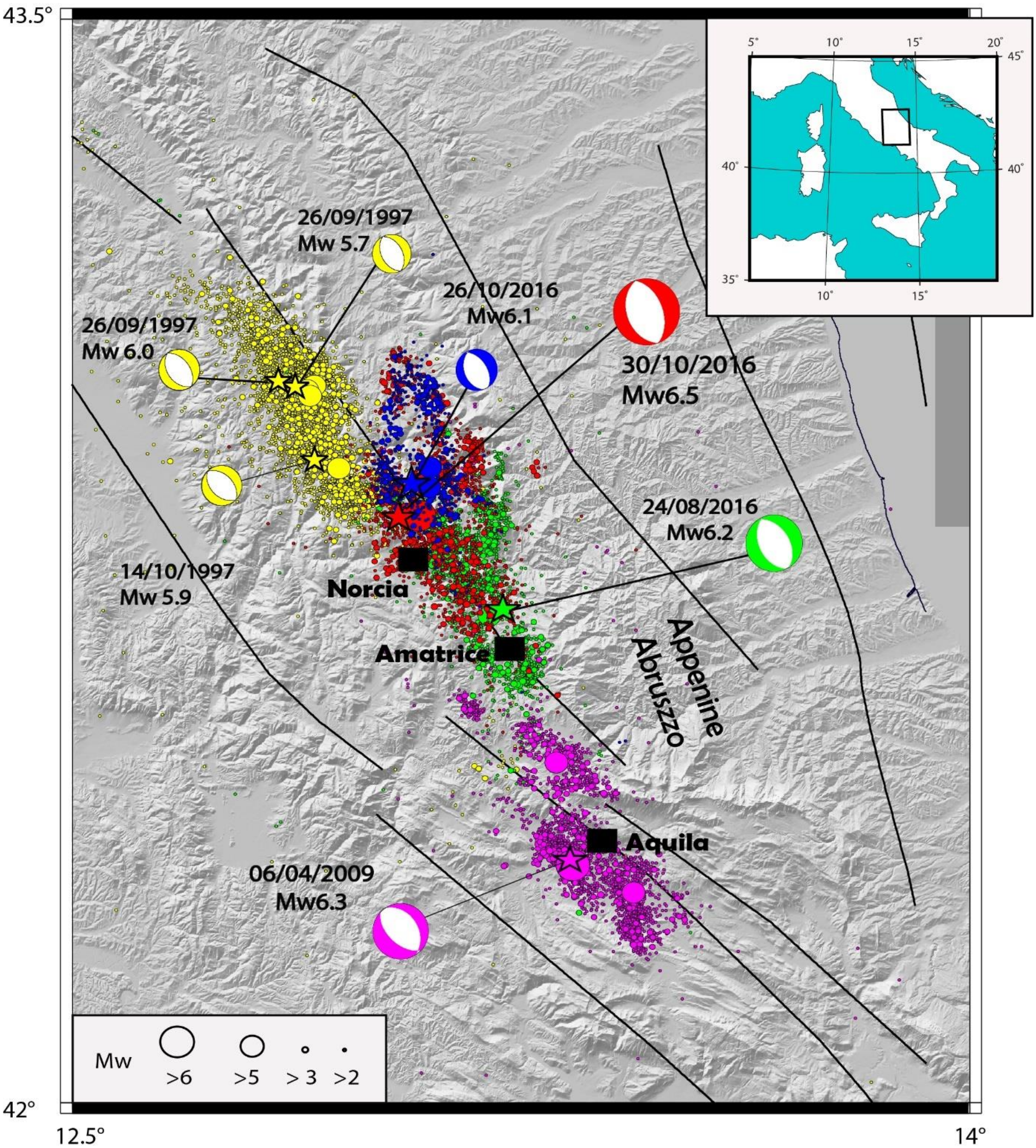

Figure 1: *Seismicity and focal mechanisms of major earthquakes occurred in the central Apennines (Italy) spanning the period from 1997 to 2016. Each earthquake sequence with a related mainshock focal mechanism is represented by specified color. For example, the magenta color represents the spatial distribution of the events associated with the 2009 L'Aquila earthquake sequence, the focal mechanism associated to the L'Aquila mainshock is also represented by the same color. The focal solutions are from the Global Centroid Moment Tensor (https://www.globalcmt.org/CMTsearch.html). The seismicity of the Central Apennine is from INGV (http://terremoti.ingv.it/en). The inset figure represents the location of the studied area. Note that the 2016 Amatrice-Norcia seismic sequence may view as a unique earthquake swarm divided into three smaller sequences. The colored data (green, blue, red) mimic the seismic migration from the August 24th (sequence in green), and culminating with the October 30th, Mw 6.5 earthquake (sequence in red).*

From the structural point of view, the evolution of fault geometry near the L'Aquila fault zone seems to be controlled by a set of conjugate EW-NS faults system in a transtentional regime at the limit of large active fault segments. The aftershock distribution analysis following the 2009 L'Aquila mainshock shows that a non-neglected part of the aftershock productivity (~ 32% of the total aftershocks recorded during the period from April to December 2009) is located at the limit of the fault slip zone. Scholz (2019) interprets this spatial distribution of the aftershocks as typical for a triggering mechanism assisted by a poroelastic and/or viscoelastic stress relaxation.

After the 2009 L'Aquila earthquake, the Central Apennine was followed by three moderate earthquakes with a magnitude M≥ 6.0: the 2016 August 24 Amatrice earthquake (Mw 6.2), the 2016 August 26 Ussita earthquake (Mw 6.1) and the 2016 October 30 Norcia earthquake (Mw

6.5). Thus, these three sequences fill the gap between the Colfiorito and L'Aquila earthquake series (Figure1). Focal mechanism of the three earthquakes shows a normal faulting solution (Figure1) consistent with a rate of 3-4 mm/yr in Apennines zones. The mechanics of deformation in the Central Appenines is complex. The strain release nearby Amatrice fault-zone is accommodate by a complex interaction between the main normal faults and a secondary structures inherited from the pre-Quaternary compressional tectonic phases (Cheloni *et al.*,2017). Pino *et al.* (2019) point out that the seismic sequences starting with the Amatrice and after Ussita earthquakes advance the triggering of the October 30 Norcia earthquake (Mw 6.5). Based on the fact that the earthquake triggering mechanism is assisted by fluids, Pino *et al.* (2019) obtain an average value of fluid diffusivity able to trigger the 2016 Amatrice-Norcia sequence equal to 1.5 10^4 cm^2/s. The values are low compared to the values obtained for the 1997 Colfiorito sequence (Antonioli *et al.*, 2005) and may explain the variability in earthquake time delay (from hours to days) between the two sequences (Figure 2A & C). In the case of the 1997 Colfiorito and the 2016 Amatrice-Norcia sequences, the difference in fluid characteristics obtained by different authors (Antonioli *et al.* 2005; Pino *et al.* 2019…) correlate with the spatial variation of the seismicity from south to north in the Central Appenine fault zone (Figure1). The spatial variation in fluid diffusivity also explains the high degree of heterogeneity along the central Appenine fault-zone and the difference in time delay between major earthquakes.

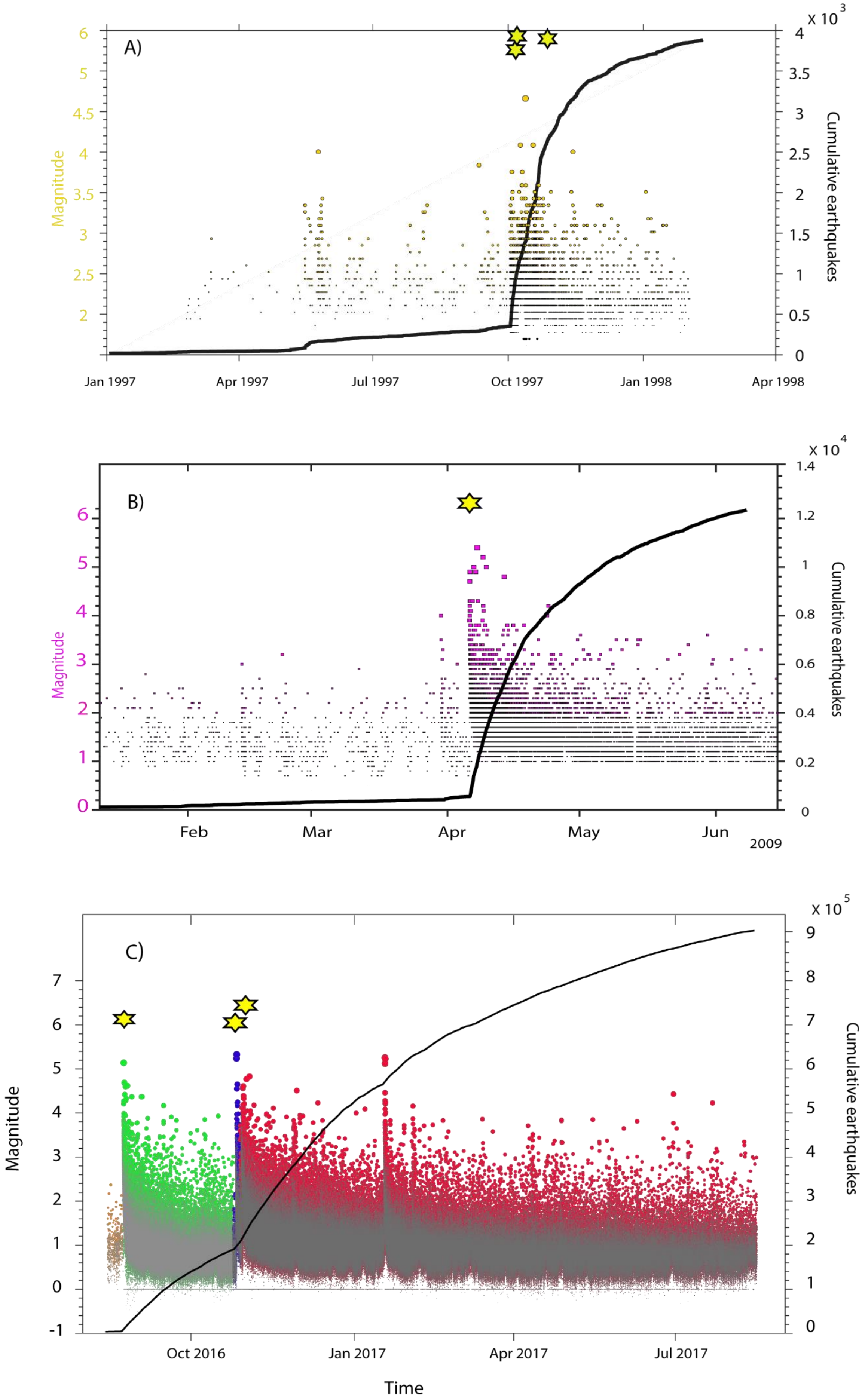
A)
Magnitude
Cumulative earthquakes
X 10^3
Jan 1997
Apr 1997
Jul 1997
Oct 1997
Jan 1998
Apr 1998
B)
Magnitude
Cumulative earthquakes
X 10^4
Feb
Mar
Apr
May
Jun
2009
C)
Magnitude
Cumulative earthquakes
X 10^5
Oct 2016
Jan 2017
Apr 2017
Jul 2017
Time

Figure 2: *Evolution of the Cumulative number of earthquakes and magnitude distribution through time for:* ***A)*** *the 1997 Colfiorito sequence,* ***B)*** *the 2009 L'Aquila sequence and* ***C)*** *the 2016 Amatrice-Norcia sequence. The earthquakes datasets used for A) and B) are from INGV. The earthquake database used for construct the C) plot is derived from a recent high precise determination of ~900, 000 earthquakes derived from deep-neural-network-based picker (Tan et a.,2021). The earthquake magnitude evolution in time from each sequence is represented by a specific color same as in Figure 1. The yellow stars represent the major events for each sequence. The Time evolution of earthquakes and related magnitude distribution are constructed using the Zmap software (Wyss & Wiemer.,2000).*

THE 2019 RIDGECREST SEQUENCE

In July 2019, two moderates to strong earthquakes with a magnitude Mw 6.4 and 7.1 struck Ridgecrest (California) in SWL-ECSZ region. Earthquake ruptures characteristics deduced from InSAR, source time functions and early aftershock analysis indicate that the Mw 6.4 and the Mw7.1 earthquakes occurred on conjugate strike-slip faults within a time interval approximately equal to 34 hours at 12 km distance and 8 to 11 km depth, respectively (Figure 3; Barnhart *et al*. 2019; Fielding *et al.* 2020…). Early surface deformation analysis deduced from Synthetic Aperture Radar Interferogram (InSAR) and focal mechanism analysis indicates that the 2019-07-04 (Mw6.4) and the 2019-07-06 (Mw7.1) events occurred on NE-SW and NW-SE trending conjugate strike-slip faults. The Ridgecrest fault zone is a part of the Indian Wells Valley, which is connected to the Central Basin and Range tectonic province. This area is bounded on the West by the Sierra Nevada Mountains, on the South by the Garlock fault, and on the East by the Walker Lane belt (Figure 3). The Little Lake (or Ridgecrest) fault zone (LLFZ) is defined as an important component of the SWL-ECSZ which accommodates a non-neglected part of the Pacific-North America plate boundary displacement (Figure 3). The seismotectonics of the Ridgecrest region reflects the complex interaction of left lateral and right lateral conjugate strike slip faults in a variable tectonic regime (Figure 3). The transition from transpressional regimes near LLFZ to transtensional regimes at the north of Ridgecrest (near Coso-Range) agrees with the rotation of the maximum principal stress (Combs 1980) and may be interpreted as a result of a large weakening mechanism of an immature faults.

Based on the poromechanical model proposed by Rice (1992), Axen (1992) interprets the active deformation along the low angle normal fault in the Indian Wells Valley – Coso Range as a consequence of a weakening mechanism due to abnormally elevated pore-fluid pressure in both brittle and ductile regime. In this case, the permeability in active fault zone must be higher than its surrounding rocks. Large volumes of fluid migrate from ductile to brittle zone in active mylonite area are also observed in relation to the detachment zones in the Central Mojave Desert (Axen 1992). The analysis of a high resolution imaging derived from satellite optical imagery shows that the presence of inelastic failure related to the 2019 Ridgecrest earthquake sequence reflects a mylonitic deformation of the fault damage zone (Barnhart *et al*.,2020). The observed mylonitic zones are directly correlated to the degree of fault maturity of the Ridgecrest conjugated ruptures. The analysis of Line of sight (LOS) interferometric Synthetic Aperture Radar (SAR) displacements following the 2019 Ridgecrest sequence attests that a part of the observed early 2019 Ridgecrest postseismic deformation is indicative of a poroelastic rebound (Wang & Bürgmann., 2020). The LOS displacements derived from both Sentinel-1 and COSMO-SkyMed (CSK) SAR data reveals that the maximum postseismic deformation along the LOS of ascending satellite tracks is located at the northwest of the Mw 7.1 epicenter near the Coso geothermal fault zone (Wang & Bürgmann, 2020). Most of the seismicity recorded before the 2019 Ridgecrest sequence is relatively small ($M \leq 3$). The largest event recorded in SWL is the 1872 M7.5 Owens Valley earthquake (Figure S1; Monastero *et al.* 2002). The 1872

M7.5 Owens Valley earthquake is dominated by a right-lateral shearing deformation along the Owens Valley fault (Figure S1). The recurrence of earthquake with a magnitude $M \geq 5.0$ in SWL is approximatively equal to 20 years with two significant sequences with four moderate events ($M \geq 5.0$) occurred near Ridgecrest city between 1995 and 1998 (Hauksson *et al.* 1995). This recurrence pattern has been culminated by the occurrence of the 2019 Ridgecrest sequence (Mw 6.4; Mw 7.1). The study of the mechanics of earthquake and fault interaction in the context of conjugate strike-slip faults indicate a clear influence of fluid migration on the occurrence of moderate to large earthquakes in the SWL tectonic domain (Kariche, 2022). Based on the Coulomb poroelastic stress change modeling approach, the time delay between two conjugate strike-slip earthquakes seems to be coupled to the variation in fluid diffusivity along heterogeneous faults (Kariche, 2022). These observations are in concordance with the Cocco & Rice (2002) Coulomb stress transfer modeling results taking into account the presence of high pore fluid pressure at hypocentral depth.

Considering the ~34 hr characteristic time delay of the 2019 Ridgecrest sequence representing the time delay between the Mw 6.4 foreshock and the Mw 7.1 mainshock (Kariche, 2022) and a fluid viscosity of $3x10^{-4}$ Pa.s, the average value of permeability necessary to trigger the Mw7.1 Ridgecrest event is estimated between 10^{-14}-10^{-15} m^2. Despite the fact that this value is higher than the value obtained by Cocco and Rice (2002) for normal fault geometries, it seems to be in a good agreement with the permeability values obtained recently by Miller (2020) for the 1992 Lander-Big Bear conjugated sequence and based entirely on the conceptual model of permeability dynamics as proposed by the same author. Also, this permeability value estimation seems to be in a good agreement with the value obtained by Nespoli *et al.* (2018) for the 2012 Emilia-Romagna earthquake sequence. The temporal and spatial evolution of major events following the Mw 6.4 foreshock sequence may explain the significant increase in the value of permeability along cracks following the Mw7.1 earthquake. Based on this assumption, the temporal distribution of earthquake frequency and related moment release must predict a temporal fluctuation of the G-R b-value during the 2019 Ridgecrest sequence caused essentially by the variation of pore-fluid pressure at depth.

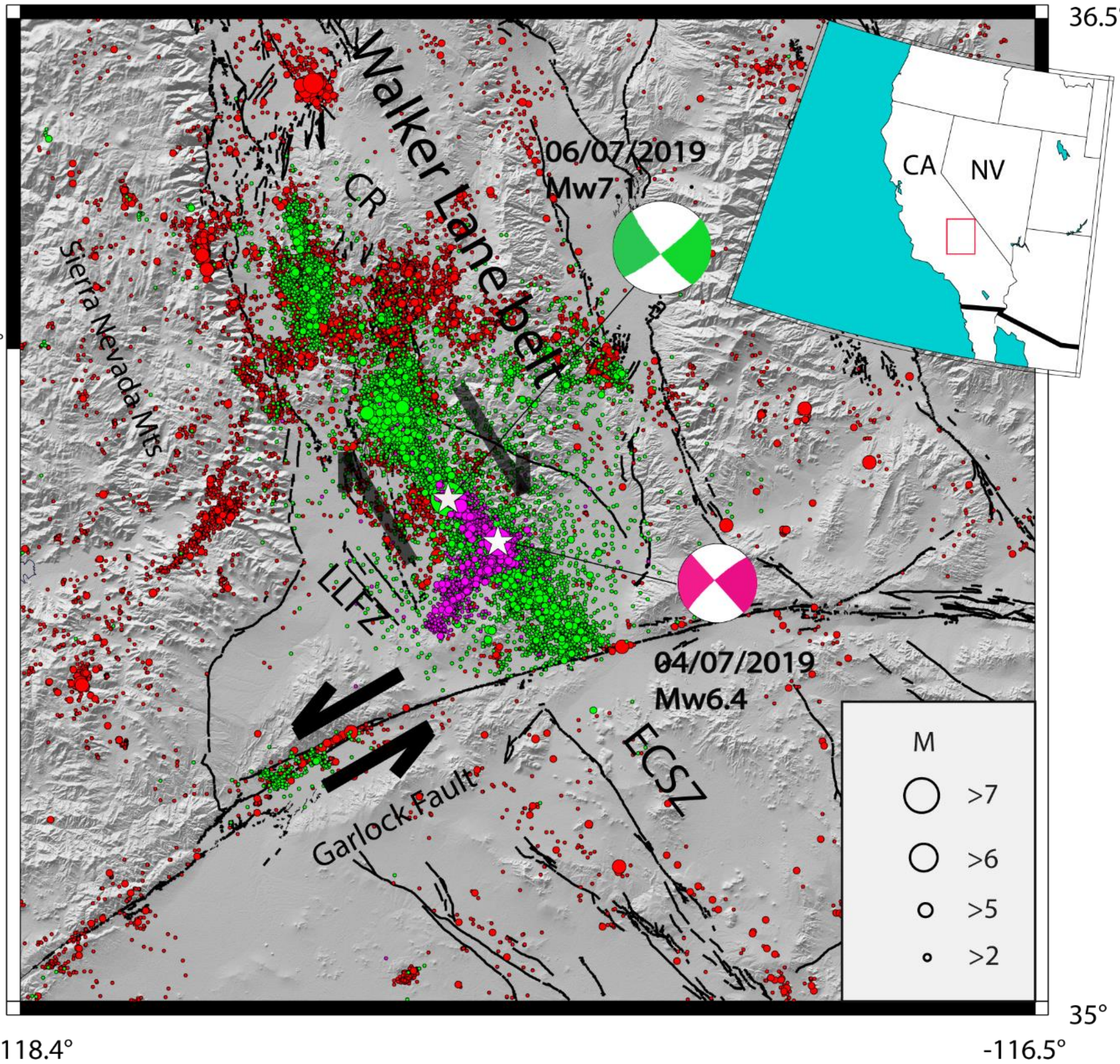

Figure 3: *Seismicity along the Southern Walker Lane (SWL)-Eastern California Shear zone (ECSZ) from 2008 to 27/10/2019 using combined SCEDC QTM catalog (Ross et al. 2019) and the high definition NEIC-USGS catalog (https://earthquake.usgs.gov/earthquakes/search/). The color circles indicate the seismicity at different periods: red from the period between 1980 and July 2019; green for the period covering the 2019 Ridgecrest foreshock activity and magenta for events following the Mw7.1 mainshock. The stars show the location of the 2019-*

07-04 (Mw6.4) and the 2019-07-04 (Mw 7.1) earthquakes. The red rectangle in the inset figure represents the studied area. LLFZ= Little Lake Fault Zone. CR= Coso Range. CA=California State. NV= Nevada State.

TEMPORAL VARIATION OF B VALUE, FORESHOCK ANALYSIS AND THE ROLE OF FLUID

As mentioned before, the high quality of seismic catalogs of the Central Apennine and Southern California regions allows us a robust estimation of the variation of cracks intensity before, during, and after a moderate to strong earthquake and therefore permits a detailed analysis of foreshocks activity prior mainshocks. The relation between the temporal variation of the b-value, foreshocks occurrence, and fluid migration shows that the decrease in b-value may correlated with the dilatancy-fluid diffusion process that precedes a large earthquake (Scholz & Kranz, 1974; Scholz, 2019). Based on a laboratory scale acoustic emissions analysis and fracture mechanics modeling of rocks failure under water-saturated conditions, the increase in stress concentration during the final stage of dilatancy and the beginning of fluid diffusion on a dominant rupture occurs when the b-value is lower than 1 (Main *et al.* 1990). The decrease in the b-value is also connected to the strain softening and shear localization during the occurrence of the foreshocks sequence (Main et al. 1990).

In order to explore in detail, the role of fluid before and after a large earthquake, I compare simultaneously the temporal evolution of the b-value in the Central Apennine with those following the 2019 Ridgecrest sequence. The analysis of the temporal evolution of the b-value includes four major sequences: the 1997 Colfiorito (Umbria Marche) sequence, the 2009 L'Aquila sequence, and the 2016 Amatrice-Norcia sequence, and the 2019 Ridgecrest sequence. To better constrain the b-value time series and as mentioned before, I use the high-resolution catalog proposed by the Istituto Nazionale Di Geofisica E Vulcanologia (INGV) combined with the Gasperini et al. (2013) and the Tan et al. (2021) catalogs for the Central Apennines and the highest confidence QTM seismicity catalog for Southern California (Ross et al. 2019) aided by the Shelly (2020) catalog for events that occurred during the 2019 Ridgecrest sequence as a seismic input to the b-value time series modeling. The b-value time series technics consists of analyzing the frequency-magnitude distribution of earthquakes over variable time windows. This approach based on a fixed number of events allows for better estimates of the variation of the b-value at each point in time which leads to better constraining the evolution of seismicity in a region with a high variation in seismicity rate through different time scales (Tormann et al., 2013). If we suppose that the b-value time series is defined as a temporal representation of crack distribution in a seismogenic zone, then the b-value magnitude for each time windows interval is selected with respect to the distribution of the magnitude of completeness (Mc). The Mc value is assessed for each window interval (with specific N=250 events) after a recutting level, established using the maximum curvature method with a correction factor of 0.2 for safety. The b-value times series is computed for selected windows using the maximum-likelihood estimates (Wyss & Wiemer, 2000). I also consider the temporal change in Mc in the b-value time series computations following each main event in order to minimize the dependence of the b-value times series from Mc in the selected time windows.

To better constrain the evolution of seismicity near Ridgecrest, I combine the QTM catalog during the entire period of 2008-2017 with the USGS seismicity catalog covering the period from January 2017 to Mai 2020. The seismicity database also includes the 2019 Ridgecrest precise relocation catalog of Shelly (2020). Similar events due to the combination of different catalogs are detected and eliminated automatically using the Zmap software (Wiemer, 2001). The Ridgecrest zone is divided into 0.15° x 0.15° grids and the events were selected using a variable time windows approach. The computation is made regarding the approach based on a fixed number of events of 250 with a 50 minimum event higher than the local value of Mc by using the Maximum curvature method with magnitude binning equal to 0.1. Considering the change in the Mc value and for the Ridgecrest earthquake sequence, I obtain an Mc value range of [0.84, 1.4] before the Mw 6.4 event and [0.66, 1.2] from the period between the Mw 6.4 and Mw7.1 mainshocks. After the Mw7.1 event, the Mc value range between [0.4, 1.2]. In order to reduce uncertainties on the b-values estimations, and as mentioned before, I asses Mc using the maximum curvature approach and I add 0.2 to the value of Mc. I confirm that the value of Mc that gives a reasonable estimate of the temporal evolution of the b-value is about 1.4, in the same order as the value proposed by Gulia et al. (2020) for the same sequence. I also verify that the temporal b-value estimates do not change considering an Mc range of [1.1,2.0]. The same approach is made for the sequences that occurred in Central Apennines.

The temporal evolution of the Mc-value with the distribution of the b-value is evaluated simultaneously at appropriate time windows in order to reduce uncertainty in the b-value estimates. The b-value time series are performed for a number of events 50 $\leq$N$\leq$500 enables us an appreciable degree of smoothing/damping signals (Figs. S8 & S9). The temporal evolution of the b-value is based on the earthquake occurrence time approach using a window size range between 50 to 500 events, which yields an interval sampling rate of approximately 1-12 months. The b-value time series shows that the shape of the time series is preserved for 100 $\leq$ N $\leq$ 500 for both the 2016 Amatrice-Norcia and 2019 Ridgecrest sequences (Figs. S8 & S9). These results are relatively the same as those obtained by Wyss & McNutt, (1998) in analyzing the 1989 earthquake swarm beneath Mammoth Mountain (CA) or by Tormann et al (2013) in the modeling of the temporal correlation between the change in the b-value and surface creep of M 6 series of events occurred in Parkfield (CA).

Figure 4 shows the preferred b-value time series for the Ridgecrest case. The optimum time series calculation is made with a sample size of 250 events at a low window overlap (~4%). Considering the Mw6.4 earthquake sequence as a Foreshock sequence, the temporal evolution of the earthquake size distribution shows an increase in b-value one year before the 2019 Ridgecrest sequence followed by a gradual decrease in b-value ~ one month before the Mw 6.4 foreshock (Figures 4 and 5). After the Mw 6.4 earthquake, the b-value rapidly varies from minimum to maximum and from maximum to minimum just before the Mw7.1 earthquake showing major double picks (Figures 4C and 5A) as predicted by the laboratory experiments in water-saturated specimens (Main et al. 1989). The sudden increase in b-value before the Mw 7.1 earthquake as observed in Figures 4 and 6A is interpreted as a response to pore pressure drop during the undrained phase of the fluid. This value is close to the value of b ~ 1 during the left lateral earthquake but the increase in aftershock productivity caused by fluid migration and pore pressure instability in the ~ 33 hours preceding the Mw7.1 right lateral earthquake tends to re-decrease the b-value to ~ 0.5 creating a double b-value minima as observed in Figures 4C, 5A, 5C and 6A.

The presence of off-fault damage accumulation and fluid redistribution tends to decrease rapidly the b-value and creates a slip instability promoting the next Mw7.1 failure (Figures 4, 5, and 6A). In this case, the minimum doublet b-value as observed in the b-value time series may be interpreted as a local dilatancy hardening phase resulting from fluid migration along conjugated fault ruptures. At this time, the fluid migration at a short time-scale requires a significant evolution of the permeability along fault ruptures. Based on this assumption and other considerations in relation to the stress change induced by fault geometries in a spring-slider model for dilating fluid-infiltrated fault (Segall & Rice, 1995; Chambon & Rudnicki, 2001), the temporal fluctuation of the b-value related to the 2019 Ridgecrest sequence seems to be controlled by slip instability due essentially to the pore pressure fluctuation caused by fluid migration along the heterogeneous fault zone.

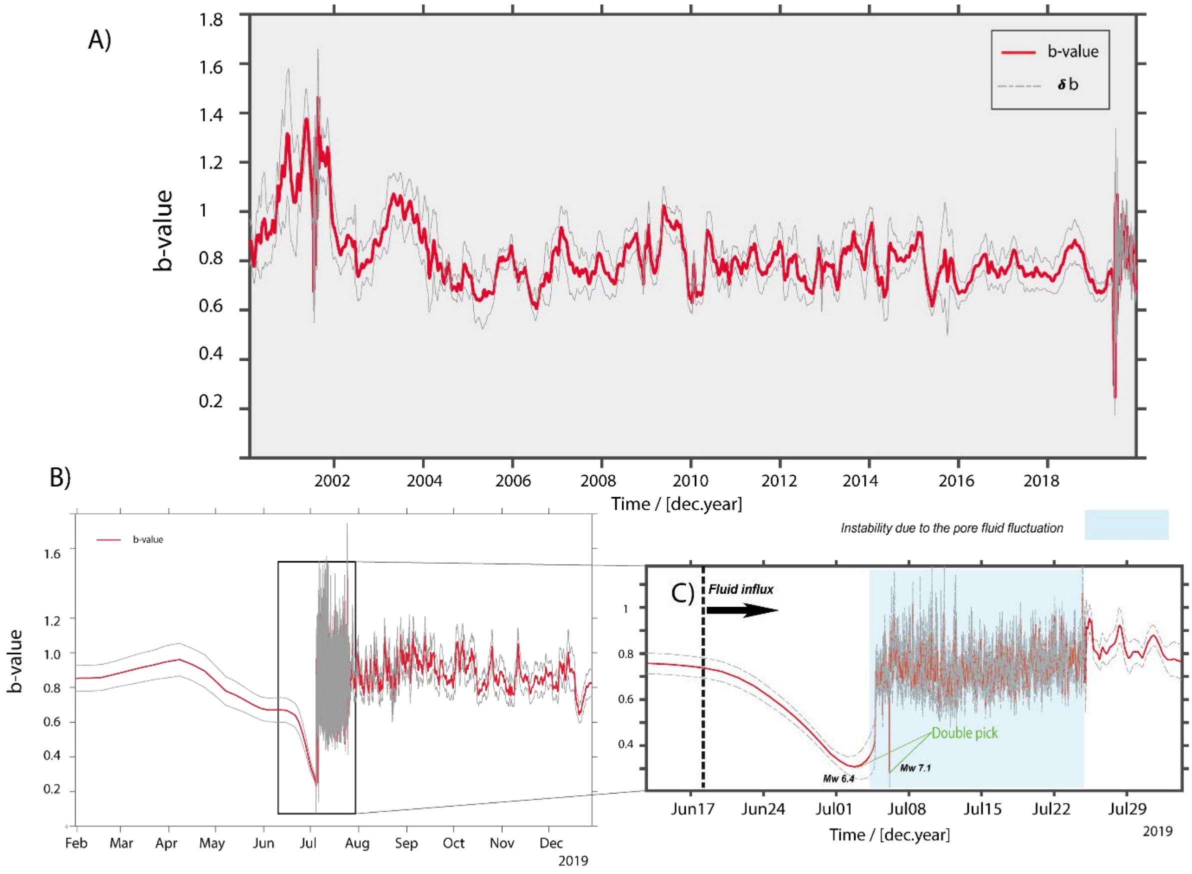

Figure 4*:* *Earthquake size distribution estimates for the Ridgecrest fault zone area.* ***A)*** *b-value time series spanning the period from 2000 to 2020 using the highest confidence QTM seismicity catalog for Southern California (Ross et al. 2019) combined with the high definition USGS-NEIC catalog. The identical events were found and automatically fixed using the Zmap software. The b-value time series were computed using the maximum curvature approach for a moving window of 500 events with a step size of 50 events. The window overlap is fixed at 4%. The Standard deviation of the b-value (δb) is represented by a dashed grey line and is obtained using the maximum likelihood estimation approach (Shi & Bolt 1982).* ***B)*** *Zoom-in figure for the period from February 2019 to January 2020.* ***C)*** *Zoom-in figure for the period from ~ 2 weeks before the 2019 Mw 6.4 first earthquake to August 01, 2020, but by adding a high smoothing plot factor (~ 6) to the b-value estimations.*

Note that the temporal b-value instability associated with the pore pressure fluctuation continues during the two months following the Mw7.1 earthquake (Figures 4B and C). The ~

two-month instability period may also represent the duration of the Mw 7.1 poroelastic rebound. Also, the similarities between the temporal evolution of the b-value for the 2019 Ridgecrest and the 2016 Amatrice-Norcia sequences (Figure 6 A and B) may suggest an analog physical mechanism controlling the foreshock occurrence for both sequences.

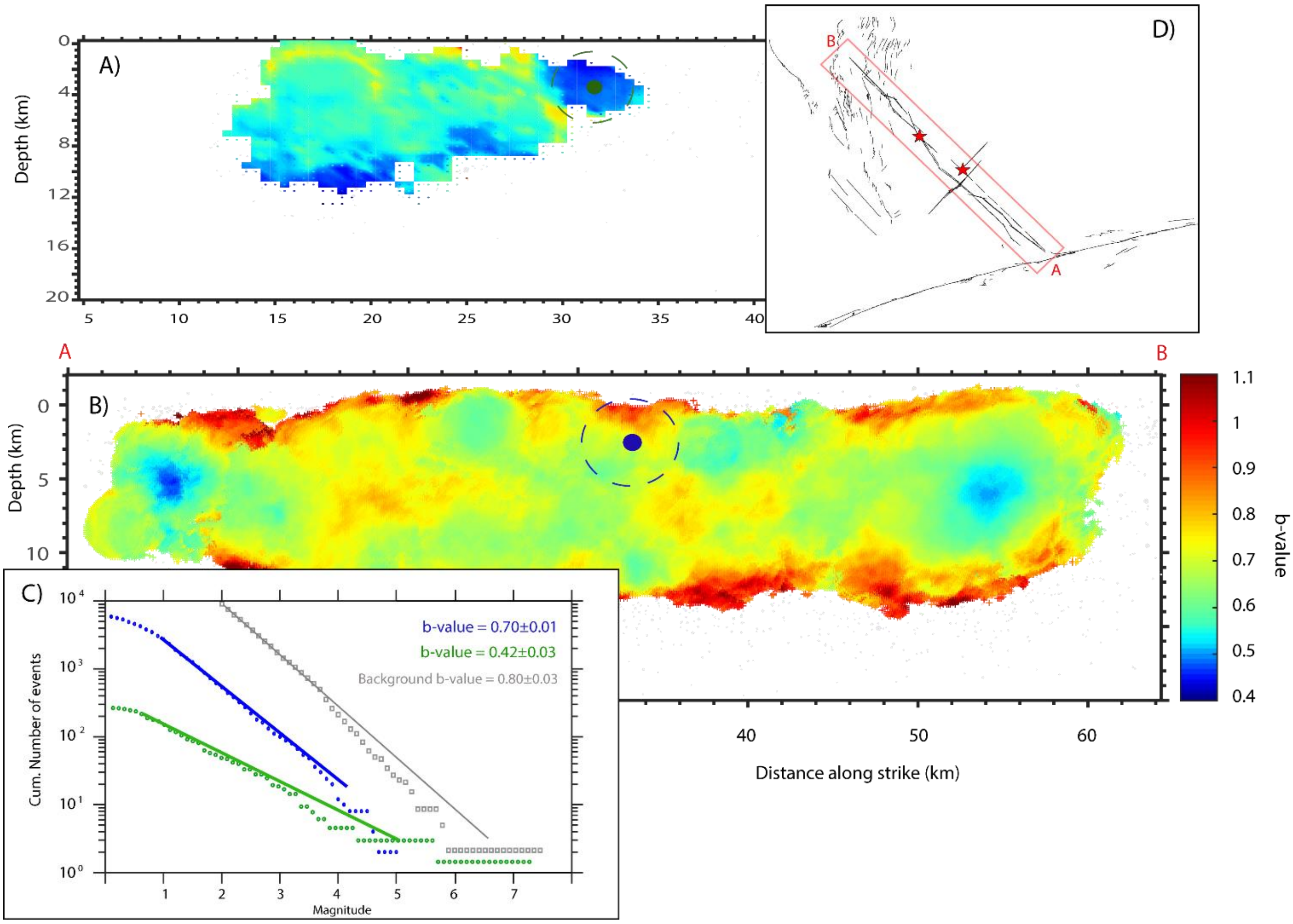

Figure 5*: Spatio-temporal evolution of the b-value associated with the 2019 Ridgecrest sequence:* ***A)*** *cross-section showing b-value distribution before the Mw7.1 earthquake.* ***B)*** *Cross-section showing a b-value distribution after the Mw7.1 earthquake.* ***C)*** *Frequency-Magnitude Distributions (FMD) around the Mw7.1hypocentral area before and after the Mw7.1 event: the green curve represents the G-R distribution before the Mw7.1 event, the blue curve represents the G-R distribution after the Mw7.1 and the gray curve represents the background FMD distribution. The dashed colored circles in A) and B) represent the locations of events used in C).* ***D)*** *Position of the cross-section with respect to*

the surface distribution of the Ridgecrest fault ruptures. The Ridgecrest Fault-ruptures are from Xu et al., (2020). *The Quaternary faults are from the USGS.*

Indeed, the b-value anomalies as in figure 6B also coincide with the hydrogeological and geological anomalies observed in the months before and during the onset of the Amatrice-Norcia sequence (Barberio et al.,2017). These anomalies are interpreted as the consequence of a deep crustal fluid migration along major active ruptures (Barberio *et al.* 2017). The hydrogeochemical changes observed in a group of springs in the central Apennines (Barberio *et al.* 2017) with the increase in the content of Cr, Fe, and V in a calcium carbonate aquifer during the months before the 2016 Amatrice-Norcia sequence also agree with the change in earthquake size distribution (Figure 6B) and denote clear evidence of fluid migration following the 2016 Amatrice-Norcia sequence. Also, the double b-value minima as observed in figure 6B correlates with the relative crustal velocity fluctuation observed in Amatrice-Norcia seismogenic zone (Soldati et al., 2019).

Considering the case of the 1997 Colfiorito sequence, the gradual decrease in b-value prior to the foreshock sequence (Figure 7C) seems to be concordant with the fracture model of Main et al. (1990). Adopting the Main et al (1990) experimental model of cracks, the temporal evolution of the b-value may be defined here as a rapid failure after periods of strain hardening and strain softening due essentially to the pore-fluid diffusion process. The dilatancy softening phase related to the 1997 Colfiorito sequence seems to be controlled by the fluid migration along fault zones where the stress intensity is highly coupled to the temporal variation in effective normal stress. Considering the Terzaghi Law, the fluid diffusion phase will play a crucial role in accelerating seismicity by decreasing the magnitude of effective normal stress acting along cracks promoting the occurrence of fast slip episodes at a short time scale.

The time evolution of the b-value following the 2009 L'Aquila sequence differs from those obtained for the 2016 –Amatrice-Norcia and the 2019 Ridgecrest sequences (Figure 6 and 8). This difference may be due to the presence of a large deep fluid reservoir near L'Aquila fault zone which maintains a high pore fluid pressure during a large period of time. Indeed, the InSAR time series analysis related to the central Appenine earthquakes reveals that the sedimentary basin nearby the L'Aquila fault zone had experienced about 10 mm of accelerating subsidence in the years prior the L'Aquila mainshock (Moro *et al.* 2017) in agreement with the observed change in the frequency of the b-value time series (Figure 8).

The accelerating subsidence is viewed as a consequence of large pre-earthquake fluid migration along the fault zone (Moro et al. 2017). Based on our estimation of the b-value (Figures 7 and 8) and ground deformation estimated from SAR imagery (Moro et al. 2017), the acceleration of subsidence is interpreted here as probably due to large dilatancy-fluid diffusion processes that control the temporal fluctuations of the b-value at a large time scale. The analysis of the Time-magnitude series shows a gradual decrease in the number of events with magnitude M<3 associated with an increase of events with magnitude >3.5 in good agreement with the change in the b-value time series (Figures 7 A and 8). A second phase with an apparent increase of small magnitude earthquakes accompanied by a decrease in the number of events with a magnitude Mw larger than 3.5 is observed in the ~ months prior to the 2009 L'Aquila mainshock (Figures 7 A and 8). The gradual increase of micro-seismic events observed in the two months prior to the L'Aquila mainshock is highly coupled with the gradual decrease in the b-value (Figure 8).

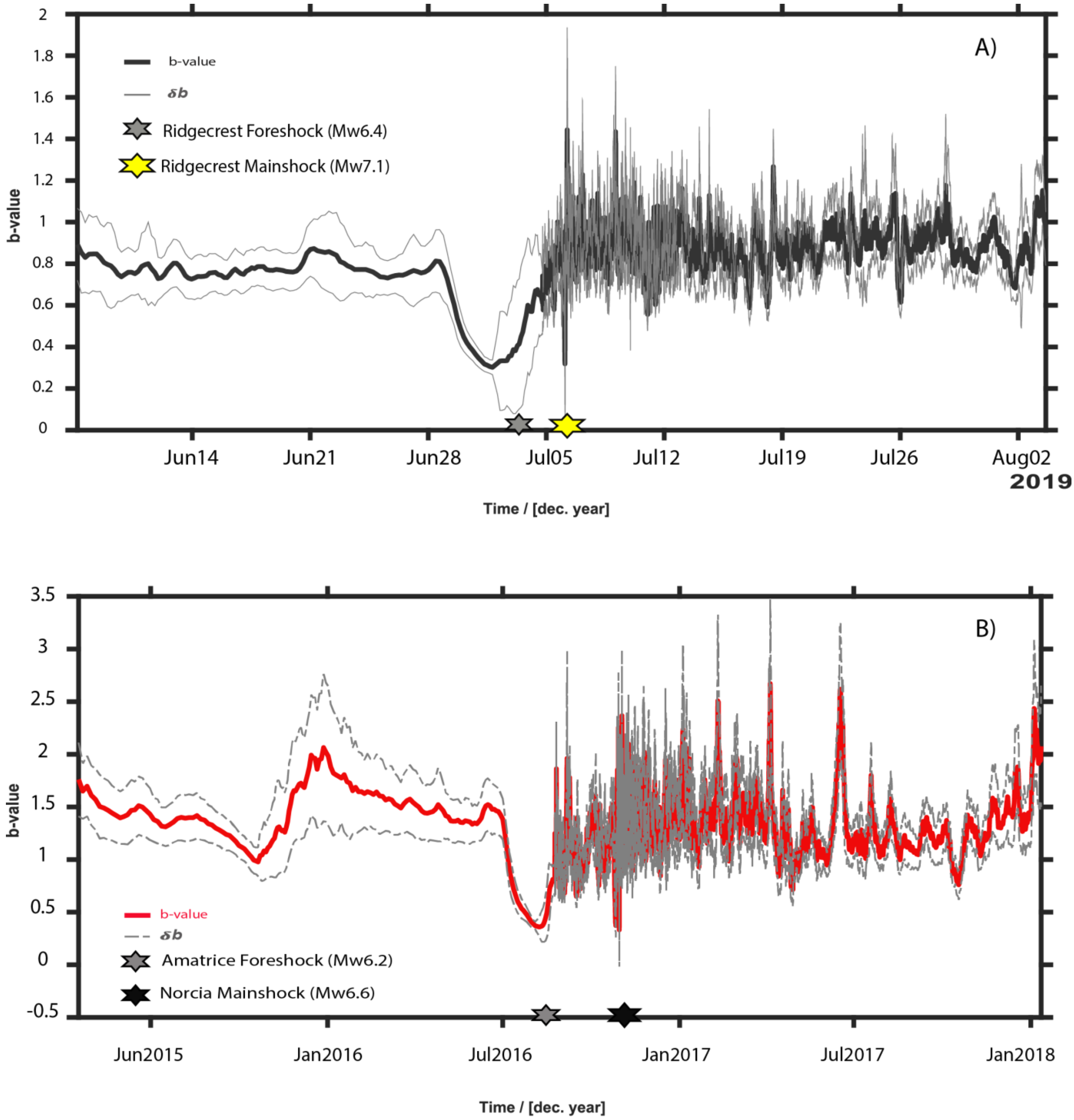

Figure 6*:* *Comparison between b-value time series analysis following:* ***A)*** *2019 Ridgecrest sequence and* ***B)*** *2016 Amatrice-Norcia sequence. The two figures show a double pick during the foreshock – mainshock period as predicted by the laboratory experiments on water saturated specimens. The b-value time series is performed using the combined high resolution NEIC-USGS catalogs and supplemented by the Shelly (2020) catalog for events that occurred during the 2019 Ridgecrest foreshock-mainshock sequence. The b-value time series for the 2016 Amatrice-Norcia sequence is performed using the entire catalog of the INGV combined with the local catalogs published by Gulia et*

al. (2019). The b-values time series are computed using ZMAP7.0. For both sequences, the uncertainty estimation is obtained by 100 bootstraps related to windows size of 200 events. The windows overlap is fixed at 2 %.

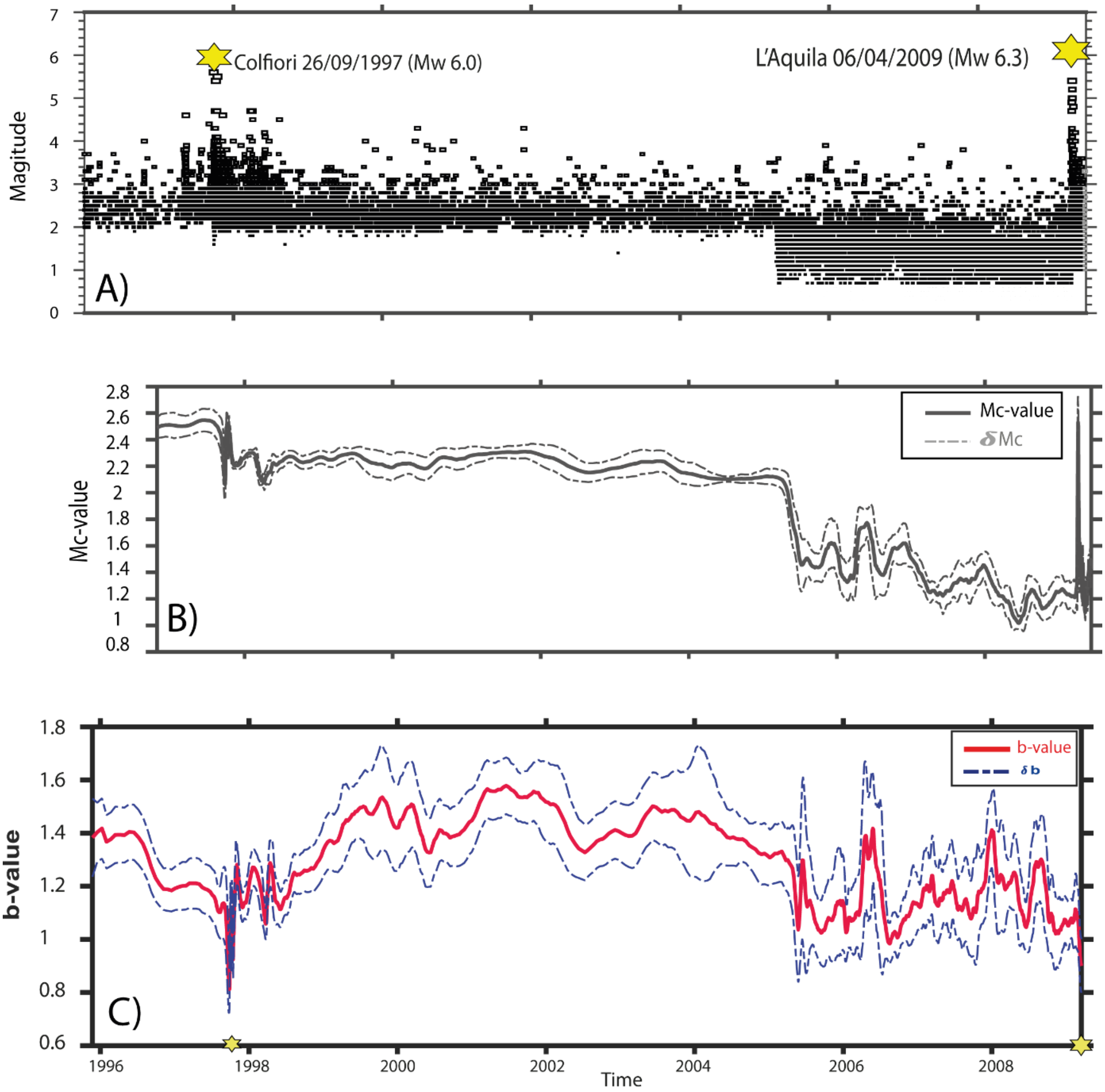

Figure 7. ***A)*** *Earthquake magnitude versus time for the central Appennines covering the periods between 1996 to 2009 and using combined catalogs of INGV and Gasperini et al (2013) catalogs. The yellow stars represent the position of the 2019 Mw 6.0 Colfiorito and the Mw6.3 L'Aquila mainshocks.* ***B)*** *Mc-value time series using the same catalogs as A) and covering the periods between 1998 to 2009.*

The magnitude of completeness (Mc) varies in times from 2.5 (before 1997) to 1.4 (after 2005) with uncertainties δMc equals to 0.15 and 0.18 respectively. ***C)*** *Temporal evolution of the G-R b-value in the central Appennines covering the same periods as in A. The shape of the b-value time series as proposed here and taking into account the temporal variation of Mc is similar to the b-value computation by supposing a fixed Mc value of 2.6 using N ~250 fixed sample size windows with 100 bootstraps.*

The tendency of the b-value time series during the last phase of the L'Aquila interseismic period is interpreted here as an influx of pore fluid into a dilatant volume near the nucleation zone. The increase in the magnitude of foreshocks just before the L'Aquila mainshock (Figure 8) affect considerably the temporal evolution of the b-value by creating a sudden drop in the b-value. The Time-shift between the start of foreshocks and the b-value decrease seems to correlate with the gradual increase in microseismic events followed by a sudden increase in earthquakes with magnitude M>=3.0 (Figure 8). This complex distribution of events may be seen as a complex evolution of the effective stress drop denoting a complex earthquake preparation conjugated to a complex distribution of the fluid flow process in a heterogeneous fault zone.

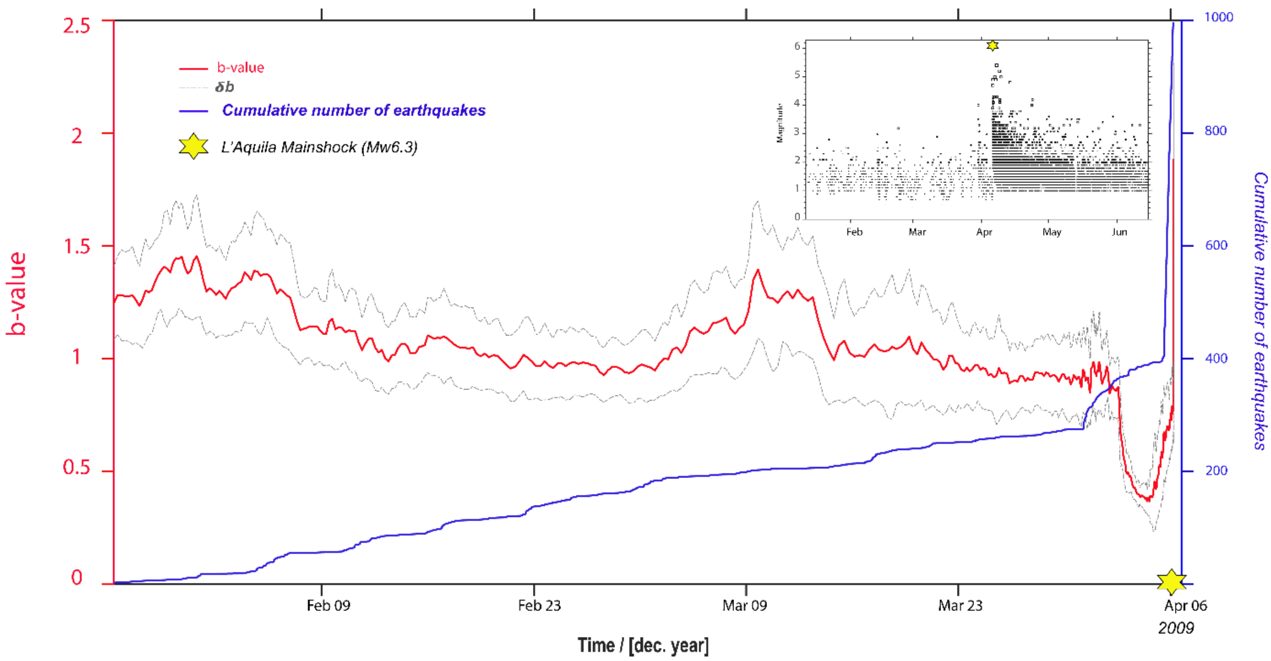

Figure 8 *Temporal evolution of the G-R b-value (in red) and the cumulative number of earthquakes (in blue) during the Foreshock period priors to the Mw6.3 L'Aquila earthquake using the entire catalogs of Gasperini et al (2013). The b-value time series is obtained using a sample windows size of 150 events with 100 bootstraps. For safety, the Mc correction value is fixed at 0.2 comparable to the value used for the predictive foreshock model of Gulia et al (2016). The black stars represent the position of the Mw 6.3 L'Aquila mainshock.*

STRESS ANALYSIS, TEMPORAL EVOLUTION OF AFTERSHOCK AND THE WEAKNESS OF ACTIVE FAULTS

As shown in the previous section, the occurrence of moderate to strong earthquakes along the SWL-ECSZ and Central Apennines zones may be coupled with the fluid migration along heterogeneous fault zones causing abnormally elevated pore pressure and promoting the occurrence of moderate to large earthquakes. Based on the Coulomb failure criterion, the dynamic poroelastic stress change modeling following the Ridgecrest Mw6.4 left lateral event shows a high value of stress at the nucleation area of the Mw 7.1 right-lateral rupture (Figure

9A) when the purely elastic stress modeling predicts an absence of earthquake activities (Figure 9B**;** Lozos & Harris, 2020; Kariche, 2022). One of the possible explanations for the temporal evolution of stress change values from negative to positive as shown in figure 9 is the fluid redistribution along conjugated fault ruptures which creates favorable conditions for a weakening mechanism by increasing pore-fluid pressure along the right-lateral major fault rupture and in fact, promoting the occurrence of the Mw7.1 earthquake. The rupturing process on conjugated strike-slip faults assisted by fluid migration is not unusual. Using a typical undrained and drained Poisson ratios for a Berea sandstone, the modeling of the Coulomb failure function per unit of stress drop caused by the 1987 Elmore-Ranche event (Mw 6.2) on the conjugated Superstition Hills fault (Mw6.6) show a maximum stress value in the ~11 hr following the Mw 6.2 event (Hudnut et al, 1989). For the 2019 Ridgecrest sequence, the Coulomb stress change modeling taking into account the effect of fluids reveals that the ~33hr time delay between mainshocks may viewed as a triggering mechanism controlled by the fluid-flow process (Figure 9A; see also figure S5 on Kariche, 2022). The value of fluid diffusivity is relatively low to the value obtained for the Superstition Hills sequence (Kariche, 2022) and may denote that the fluid migration along faults controls the time delay between earthquakes.

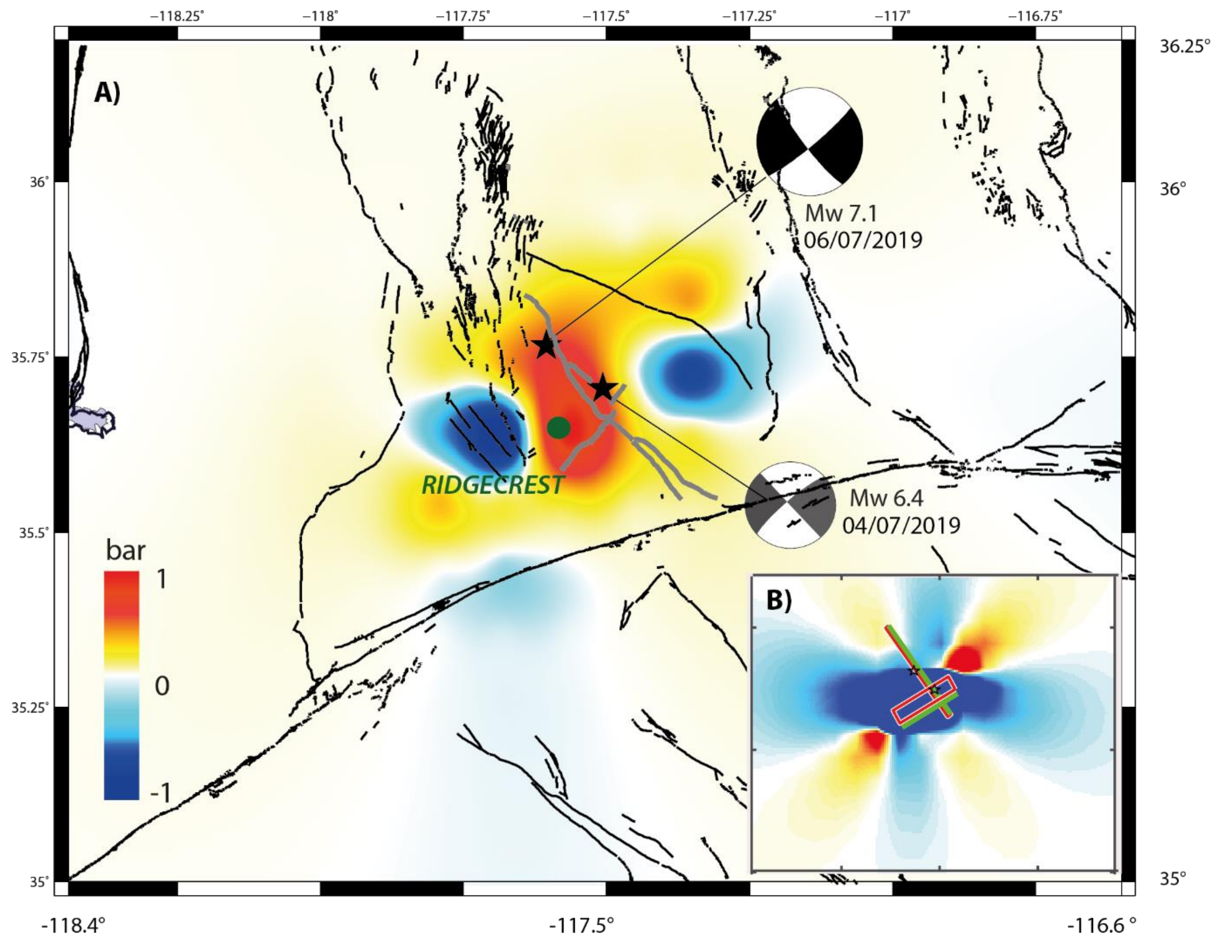

Figure 9: ***A)*** *Short–term poroelastic stress change modeling following the Mw6.4 earthquake on receiver fault planes with Strike /Dip/ Rake = 143°/85°/-165° at 8km depth. The post-seismic stress redistribution following the 04-07 (M6.4) from the undrained state to the drained fluid state using extreme undrained and drained Poisson ration values (υu, υ = 0.31, 0.15). These values are interpreted as a consequence of a high variation in rock rheology before and during the Mw6.4 earthquake.* ***B)*** *Co seismic stress transfer caused by the Mw6.4 earthquake on receiver fault planes with Strike /Dip/ Rake = 143°/85°/-165 at 8 km depth. The co-seismic stress modeling is performed using simple conjugate fault geometries.*

Considering a model of friction which assumes that the frictional stress σ_f is proportional to the shear stress magnitude after an earthquake, and if we argue that the stress difference following an earthquake is coupled to the radiated wave energy E_s , then an average dynamic stress drop $\Delta\overline{\sigma_d}$ can be expressed by using the simple solution as (Kanamori ,1994):

$$\Delta\overline{\sigma_d} = \frac{E_s\ (J)}{M_0\ (N.m)} \times 2\mu \ldots\ldots(9)$$

where μ is the rigidity and M_0 is the seismic moment.

The radiated energy can be estimated by using the equation (Kanamori, 1994):

$$E_s\ (J) = \frac{1}{2}\ S\overline{D}\ (\sigma_0 - \sigma_1).\ \ldots\ldots..(10)$$

where S represents the surface area of the crack, $\overline{D}$ represents the average crack displacement during an earthquake and the $\sigma_0 - \sigma_1$ is defined as the differential stress. The value of $E_s\ (J)$ can also be obtained directly by analyzing the seismic wave form.

By using equation 9 and 10 for a value of M_0 and Es deduced from the 2019 Ridgecrest source time functions extracted from the Incorporated Research Institutions for Seismology (IRIS), I estimate an average dynamic value of stress drop for the Mw 7.1 Ridgecrest earthquake as equal to $\Delta\sigma_d$ ~ 20 bars for a coefficient of rigidity ~ 3.10^{11} dyne/cm^2. This value is ~ three times less than the value of static stress drop Δσs for the same event obtained by joint focal mechanism, GPS , and InSAR data (Barnhart *et al.* 2019; Sheng & Meng 2020). The value of $\Delta\sigma_d$ for the Ridgecrest main event is relatively low compared to those obtained by Shearer *et al.* (2006) for the major earthquakes that occurred in Southern California. Even so, the temporal anisotropy in stress drop following Ridgecrest (from static to dynamic) concurs with spatial heterogeneity in the stress drop along the SWL-ECSZ (Shearer *et al.*,2006; Hauksson, 2015). The analysis of a large set of focal mechanisms in the SWL-ECSZ shows a high anisotropy in stress drop distribution from the Garlock fault zone to Ridgecrest (Hauksson, 2015). The stress drop starts low near the left lateral Garlock fault, increases to the northwest near Ridgecrest faults, and finally, reaches the minimum at the Coso geothermal area (Hauksson, 2015). Also, the spatial variation in stress drop is in good agreement with the rotation of the maximum horizontal stress (SHmax) (Yang & Hauksson, 2013). The variation in stress drop combined with the SHmax rotation may suggest the presence of weak zones outside the Ridgecrest conjugate fault systems which are probably connected to an abnormal fluid pressure due to fluid migration at depth. According to the time-dependent composite model of Kanamori (1994), the decrease in stress drop from static to dynamic following the Mw7.1 Ridgecrest earthquake may be interpreted as a result of a dynamic weakening mechanism caused essentially by abnormal fluid pressure. In this case, the stress drop starts in the same order as the static stress drop and decreases in time during the pore-fluid pressure redistribution.

The elevated pore pressure due to the fluid migration in heterogeneous fault zone tends to affect the value of permeability and creates an area with a low-stress drop tendency. Based on the poromechanical model of Byerlee (1992), I found that the permeability along the Ridgecrest fault zone increases by a factor of 10^3 following the Mw7.1 mainshock. Similar results including causative relations between the evolution of pore-fluid pressure and the variation in stress drop are also found in analyzing stress anomalies on major active faults in Southern California (Bird, 2017) and in fault strength analysis of active fault ruptures (Copley, 2018). Based on these considerations, the temporal and spatial evolution in stress drop can not only be explained by the variation of the frictional property of rocks. Our results tend to validate the role of fluid in controlling both nucleation and the size of major fault ruptures in the SWL-ECSZ (Tong et al., 2021; Kariche, 2022). Note that the possible role of pore pressure variation on the complex distribution of stress drop during the 2019 Ridgecrest sequence was also examined by Trugman, (2020).

The fluid migration during an earthquake may also affect the productivity of aftershocks. Figure 10 shows a comparison between the cumulative stress change modeling caused by the full poroelastic relaxation of the Mw7.1 Ridgecrest using different values of drained υ and undrained υu Poisson ratio and the spatial distribution of aftershocks following the Mw7.1 Ridgecrest earthquake. Figure 10 (A, B, and C) shows a correlation between: 1) the evolution of stress change following the Mw 7.1 earthquake, 2) the fluid diffusion process and 3) the spatial distribution of a part of aftershocks nearby and at NNW of the Mw7.1 epicenter. The values of υu and υ used in Figure 10 might be associated with water-saturated rocks in the upper few kilometers of the seismogenic zone ($h \leq$ 15km). The fluid-diffusion process associate to the 2019 Ridgecrest sequence is supposed to act locally (Figures 9 and 10). The Coulomb stress change modeling result at half of the seismogenic zone and taking into account the diffuse effect of fluids shows an increase in stress change values near the epicentral area of the Mw7.1 event (Figure 9A). Also, the full poroelastic relaxation caused by the Mw7.1 of faults parallel to the main rupture seems to mimic the spatial distribution of aftershocks at the northern part of the Mw7.1 main rupture (Figure 10A, B, and D). On the contrary, for the southern part of the Mw7.1 Ridgecrest fault zone, the triggering mechanism seems to be independent of the fluid diffusion process (Figures 10 A, B, and C). These results agree with the idea that the aftershocks generation following the 2019 Ridgecrest earthquake is complex and may relate to both afterslip and poroelastic relaxation processes. Indeed, the analysis of the co and the early postseismic surface deformation (~ 2 months of deformation) following the 2019 Ridgecrest shows that the ~ one month observed postseismic deformation is associated with both afterslip and poroelastic rebound (Wang & Bürgmann, 2020). Based on the surface deformation analysis (Wang & Bürgmann, 2020) and stress change modeling results (Figure 10), I suggest that the seismicity rate associated with the southern part of the Mw7.1 main fault is mainly defined as a model based on afterslip evolution as reported by the time series analysis from the B921 strainmeter located in the same area (Hirakawa & Barbour, 2020) while the early aftershock generation in the northern part seems to be mainly due to the poroelastic rebound of the Mw7.1 mainshock (Figure 10 B and D).

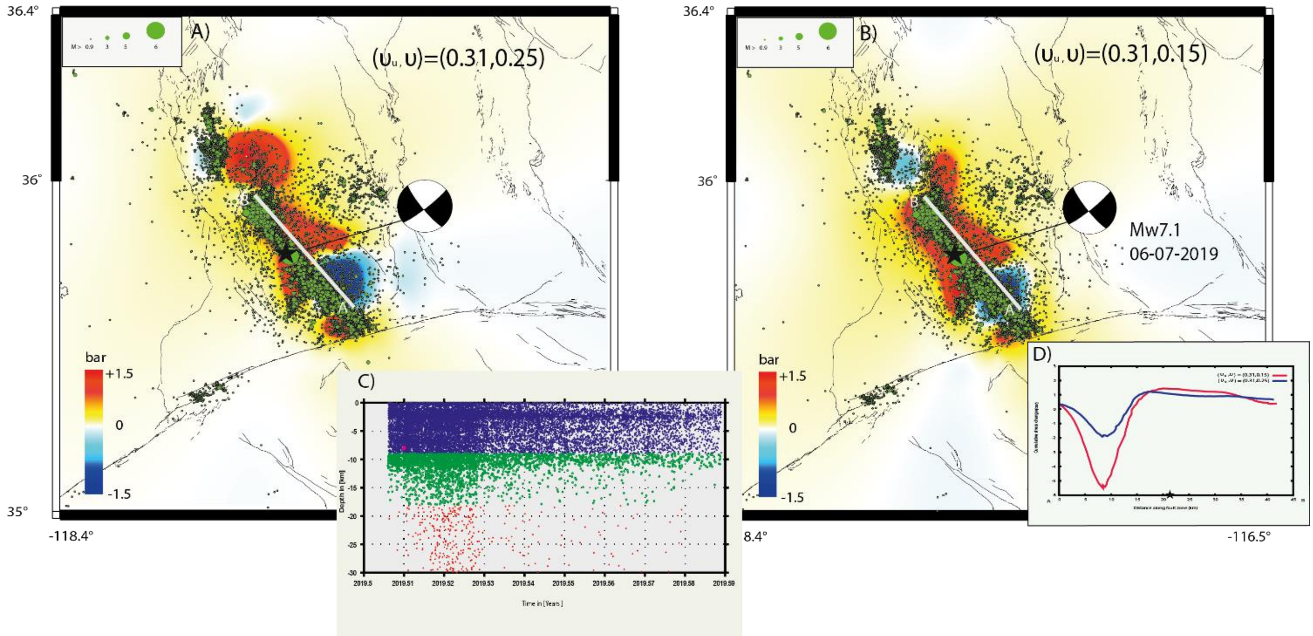

Figure 10: *Cumulative stress change due to the full poroelastic rebound following the Mw7.1 Ridgecrest earthquake on right lateral fixed receiver fault planes parallel to the Mw7.1 main rupture. A) poroelastic stress change modeling using a typical value of undrained and drained Poisson ratio(υu,υ)=(0.31,0.25). B) poroelastic stress change modeling using the extreme value of undrained and drained Poisson ratio (υu,υ)=(0.31,0.15). C) Temporal evolution of seismicity at depth following the 06-07-2019 (Mw 7.1) mainshock. D) Poroelastic stress change profiles caused by the full relaxation of the Mw7.1 earthquake along parallel right-lateral fault ruptures. The seismicity databases are from NEIC-USGS. The stress change modeling is fixed at 8 km depth.*

In order to explore in detail, the mechanism of post-seismic deformation following the 2019 Ridgecrest sequence and related fluid migration, I analyze the temporal evolution of the aftershock frequency rate associated with the Mw7.1 earthquake and I compare it with the case of the central Apennines. Figure 11 shows a comparison between the effect of fluid redistribution on aftershocks occurrence following the Mw6.0 Colfiorito and the Mw7.1 Ridgecrest earthquakes. Figure 11 (A and C) shows strong similarities between the temporal evolution of the aftershock sequence following the two earthquakes (Figure 11 A and C). The aftershock frequency rate curve starts with a rate decay of 1/√t, while it became equal to 1/t in days to one month after the 1997 Colfiorito and Mw7.1 Ridgecrest mainshocks as predicted by the pore-fluid diffusion equation (see equation 8 in the methodology section). Based on the pore fluid flow hypothesis, the 1/√t decay is interpreted as an increase in aftershocks productivity due to the pore fluid diffusion along the fault zone. Figure 11C shows that at a short-time scale, a part of the aftershocks productivity is controlled by the fluid migration along the fault zone creating an aftershocks expansion area inside and outside the main Ridgecrest fault plane. The increase in aftershocks productivity is also observed in Omori fit curve when the seismicity rate shows additional aftershocks in the ~ 10-20 days after the Mw6.0 Colfiorito and in the ~ 5-20 days after the Mw7.1 Ridgecrest mainshock (Figure 11B and D) which cannot be explained by the aftershock rate decrease as predicted by the Omori Law. These results are also validated by the abnormalities in aftershock activity observed in monitoring the temporal and spatial seismic activity following the Mw 6.4 Ridgecrest earthquake (Ogata & Omi, 2020). In addition, the duration of the increase in aftershocks activity (Figure 11D) seems to follow the duration of pore-fluid instability as estimated by the b-value time series (Figure 4C). Note that the underproduction of aftershocks as seen just after the Mw7.1 mainshock (Figure 11C) may due to the under-reporting of small events in relation to the incompleteness of the seismic catalogs soon after mainshock.

The spatiotemporal distribution of aftershocks following the 2019 Ridgecrest earthquake is complex (Ross *et al.* 2019; Trugmaan 2020). The complex slip distribution and the heterogeneity in fault zone tend to maintain elevated fluid pressure and in fact, increase aftershock productivity. These results are also valid for the Central Apennines sequences.

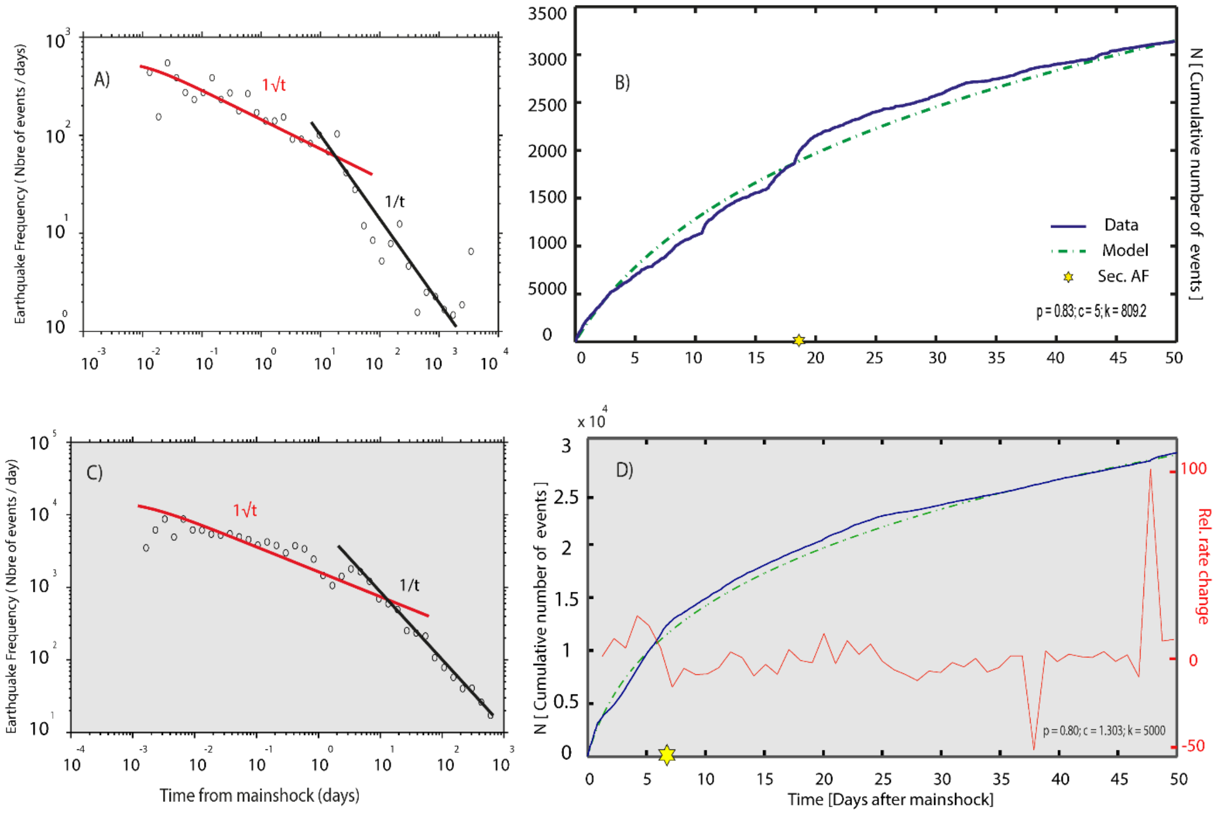

Figure 11: *Representation of the temporal postseismic effect following the Mw 6.0 Colfiorito and Ridgecrest earthquakes.* ***A)*** *Seismicity rate change versus time following the Mw 6.0 Colfiorito earthquake.* ***B)*** *Comparison of observed seismicity (blue) and the Omori fit (green) using the Zmap algorithm for 50 days' time windows following the Mw6.0 Colfiorito mainshock.* ***C)*** *Seismicity rate change versus time following the Mw 7.1 Ridgecrest earthquake.* ***D)*** *Comparison of observed seismicity (blue) and the Omori fit (green) following the Mw7.1 Ridgecrest mainshock using the Zmap algorithm for 50 days' time windows. For the aftershock frequency vs time curves, the value of c is fixed to 0.01 d for Panels A and C and suppose variable (from 2.4 to 5) for Panels B and D. The yellow stars represent the position of the second major choc for each sequence. The relative earthquake rate change (red curve in D) is obtained from the change in slope of the cumulative number curve using a Habermann function regardless of the time of greatest change and comparing the rate in the two parts of the period (before and after the division point) by fit-time windows function (Wyss & Habermann, 1988;*

Wyss & Wiemer 2000), the time variation function defines the variation between the rate before and after at local time-scale.

DISCUSSION AND CONCLUSIONS

The high quality of the Southern California and central Apennines earthquake catalogs offers us the possibility to study in details the evolution of seismicity and related fluid migration at different time scale. The evolution of seismicity near Ridgecrest and central Apennines reveals that the temporal variation in b-value is probably due to the stress-fluid redistribution along active faults. The b-value time series modeling shows a gradual decrease in the b-value for all sequences. Based on previous laboratory experiments on water-saturated specimens (Main *et al.*, 1990; Sammonds *et al*., 1992; Proctor et al., 2020), the gradual decrease in the b-value may be interpreted as a dilatancy softening mechanism caused by an increase in pore fluid pressure before each seismic event. The remarkable similarities between the evolution of the b-value following the 2019 Ridgecrest and the 2016 Amatrice-Norcia sequences represented by two b-value minima are probably due to similarities in mechanisms controlling the temporal evolution of foreshock-mainshock sequences. The duration of the first b-value peak scale with the magnitude of the first foreshock while the duration of the second peak (33 hr for Ridgecrest and 4 days for Amatrice-Norcia) appears to be independent of the magnitude of related foreshocks-mainshocks. Based on the coupled b-value –stress intensity laboratory experiments, the duration of the second picks may be interpreted as a short term poroelastic stress redistribution following a fast slip episode. Also, the temporal evolution of b-value for the Ridgecrest and the central Apennines fault zone seems to be in good agreement with the fracture mechanics model of water-saturated specimens as proposed by Main *et al.* (1989) who predict an increase in acoustic emission rate in the dilatancy fluid diffusion phase when the static and dynamic stress drop are not necessarily equals. My estimation of the average dynamic stress drop following the 2016 Ridgecrest earthquake is three times less than the static stress drop obtained by Barnhart *et al.* (2019) from joint focal mechanism and GPS and InSAR data. Based on a direct measurement of pore pressure by using a miniature pressure transducer placed on hydraulically faults network, Proctor *et al.* (2020) show that the effect of pore fluid pressure variation exerts a fundamental control on earthquake rupture initiation and may exceed the change from static to dynamic frictional properties of ruptures as predicted by the rate and state friction laws.

The idea that the fluids affect the change in the b-value is not inevitably contradicting the explanation proposed by different authors that the b-value may act as a stress meter (e.g Goebel et al., 2013; Scholz, 2015). The conceptual models proposed here suppose that the decrease in the b-value before foreshock is followed by an acceleration in crack growth and eventually an increase in differential stress over time. The only difference may relate to the modeling of the stress evolution from the period between foreshock and mainshock where the acceleration of crack front would expect a decrease in elastic stress. At this time, the decrease in elastic stress is compensated by the increase in pore fluid pressure in time and therefore increases the Coulomb stress change on the receiver faults responsible for large rupturing process. In this study, the elevated pore-fluid pressure due to the fluid migration in heterogeneous fault zone tends to affect the value of permeability and creates an area with a low stress drop tendency. Also, the occurrence of the Mw7.1 Ridgecrest right-lateral earthquake is not necessarily associated with the presence of a large deep fluid reservoir. The rapid fluctuation of the b-value just before the Mw7.1 may denote a rapid influx of fluid from surrounding rocks creating a pore fluid instability on nearby heterogeneous fault ruptures. The temporal evolution of fault permeability and related pore-fluid diffusion appears to be a crucial element in the apprehension of the difference in the time delay between earthquakes in the central Apennines and the SWL-ECSZ. The variation in earthquake time delay from hours to days for our studied sequences is in good agreement with the values of fluid diffusivity obtained following: the 1997 Colfiorito, the 2016 Amatrice-Norcia, and the 2019 Ridgecrest sequences.

In the same register, Gulia *et al.* (2020) developed a real-time earthquake monitoring system based on a traffic–light classification that uses the temporal change in b-value to constrain whether an ongoing earthquake sequence represents a decaying aftershocks phase or precursors to an upcoming large event. Dascher-Cousineau *et al.* (2020) published a paper that points out that the methodology proposed by Gulia *et al*. (2020) gives results in terms of evaluating the risk of a large impending earthquake during the Mw6.4 Ridgecrest foreshock, this method fails to predict the onset of the Mw7.1 sequence. Also, Dascher-Cousineau *et al*. (2020) show that for the case of the 2019 Ridgecrest sequence, anomalous earthquake productivity in adjacent regions may affect the background b-values and generate a false alarm. In this study, the b-value time series interpretation taking into account the poroelastic properties of the seismogenic zone shows difficulties to establish a good correlation between the duration of the foreshock activities and the magnitude of the next largest expected earthquake. Despite the fact that the inverse dependency of the b-value and the applied stress appears to be a reasonable interpretation of the b-value drop prior to the Italian and Californian sequences (Gulia & Wiemer, 2019; Gulia et al. 2020), the fluctuations of the b-value following the 2019 Ridgecrest and 2016 Amatrice foreshock sequences characterized by a double minimum seem to unfollow the hypothesis that the drop in the b-value before mainshocks is only due to the presence of high-stress levels on receiver main ruptures. This means that the magnitude of the large expected earthquake is probably controlled by the variations in pore-fluid pressure rather than the maximum differential stress.

Based on our results, detailed knowledge of geological structures, substratum permeability and a robust evaluation of the pore fluid effect with a better constrain of seismicity and strain rate before and during seismic sequences in addition to the statistical forecast methods appears to be fundamental for the seismic hazard assessment and any decision making.

DATA AVAILABILITY STATEMENTS

The data underlying this article are available in the article and in its online supplementary material.

REFERENCES

Abramowitz, M., & Stegun, I. (1970). Dover. *Handbook of mathematical functions*.

Aki, K. (1965). Maximum likelihood estimate of b in the formula log N= a-bM and its confidence limits. *Bull. Earthq. Res. Inst., Tokyo Univ.*, *43*, 237-239.

Amato, A., Azzara, R., Chiarabba, C., Cimini, G., Cocco, M., Di Bona, M., Margheriti, L., Mazza, S., Mele, F., & Selvaggi, G. (1998). The 1997 Umbria-Marche, Italy, earthquake sequence : A first look at the main shocks and aftershocks. *Geophysical Research Letters*, *25*(15), 2861-2864.

Antoine, S. L., Klinger, Y., Delorme, A., Wang, K., Bürgmann, R., & Gold, R. D. (2021). Diffuse deformation and surface faulting distribution from submetric image correlation along the 2019 Ridgecrest, California, ruptures. *Bull. Seismol. Soc. Am.*, *5*, 2275-2302.

Antonioli, A., Piccinini, D., Chiaraluce, L., & Cocco, M. (2005). Fluid flow and seismicity pattern : Evidence from the 1997 Umbria-Marche (central Italy) seismic sequence. *Geophysical Research Letters*, *32*(10).

Axen, G. J. (1992). Pore pressure, stress increase, and fault weakening in low-angle normal faulting. *Journal of Geophysical Research*, *97*(B6), 8979. https://doi.org/10.1029/92JB00517

Barberio, M. D., Barbieri, M., Billi, A., Doglioni, C., & Petitta, M. (2017). Hydrogeochemical changes before and during the 2016 Amatrice-Norcia seismic sequence (central Italy). *Scientific reports*, *7*(1), 1-12.

Barnhart, W. D., Hayes, G. P., & Gold, R. D. (2019). The July 2019 Ridgecrest, California Earthquake Sequence : Kinematics of Slip and Stressing in Cross-Fault Ruptures. *Geophysical Research Letters*, *0*(ja). https://doi.org/10.1029/2019GL084741

Berg, E. (1968). Relation between earthquake foreshocks, stress and mainshocks. *Nature*, *219*(5159), 1141-1143.

Bird, P. (2017). Stress field models from Maxwell stress functions : Southern California. *Geophysical Journal International*, *210*(2), 951-963. https://doi.org/10.1093/gji/ggx207

Cappa, F., Scuderi, M. M., Collettini, C., Guglielmi, Y., & Avouac, J.-P. (2019). Stabilization of fault slip by fluid injection in the laboratory and in situ. *Science advances*, *5*(3), eaau4065.

Chambon, G., & Rudnicki, J. W. (2001). Effects of normal stress variations on frictional stability of a fluid-infiltrated fault. *Journal of Geophysical Research: Solid Earth*, *106*(B6), 11353-11372.

Cheloni, D., De Novellis, V., Albano, M., Antonioli, A., Anzidei, M., Atzori, S., Avallone, A., Bignami, C., Bonano, M., Calcaterra, S., Castaldo, R., Casu, F., Cecere, G., De Luca, C., Devoti, R., Di Bucci, D., Esposito, A., Galvani, A., Gambino, P., … Doglioni, C. (2017). Geodetic model of the 2016 Central Italy earthquake sequence inferred from InSAR and GPS data. *Geophysical Research Letters*, *44*(13), 6778-6787. https://doi.org/10.1002/2017GL073580

Chen, C.-T., Chan, Y.-C., Beyssac, O., Lu, C.-Y., Chen, Y.-G., Malavieille, J., Kidder, S. B., & Sun, H.-C. (2019). Thermal History of the Northern Taiwanese Slate Belt and

Implications for Wedge Growth During the Neogene Arc-Continent Collision. *Tectonics*, *38*(9), 3335-3350. https://doi.org/10.1029/2019TC005604

Chiaraluce, L. (2012). Unravelling the complexity of Apenninic extensional fault systems : A review of the 2009 L'Aquila earthquake (Central Apennines, Italy). *Journal of Structural Geology*, *42*, 2-18.

Chiaraluce, L., Ellsworth, W., Chiarabba, C., & Cocco, M. (2003). Imaging the complexity of an active normal fault system : The 1997 Colfiorito (central Italy) case study. *Journal of Geophysical Research: Solid Earth*, *108*(B6).

Cocco, M., & Rice, J. R. (2002). Pore pressure and poroelasticity effects in Coulomb stress analysis of earthquake interactions. *Journal of Geophysical Research: Solid Earth*, *107*(B2), ESE-2.

Combs, J. (1980). Heat flow in the Coso Geothermal Area, Inyo County, California. *Journal of Geophysical Research*, *85*(B5), 2411. https://doi.org/10.1029/JB085iB05p02411

Copley, A. (2018). The strength of earthquake-generating faults. *Journal of the Geological Society*, *175*(1), 1-12. https://doi.org/10.1144/jgs2017-037

Dascher-Cousineau, K., Lay, T., & Brodsky, E. E. (2020). Two foreshock sequences post Gulia and Wiemer (2019). *Seismological Society of America*, *91*(5), 2843-2850.

De Barros, L., Cappa, F., Deschamps, A., & Dublanchet, P. (2020). Imbricated aseismic slip and fluid diffusion drive a seismic swarm in the Corinth Gulf, Greece. *Geophysical Research Letters*, *47*(9), e2020GL087142.

Deschamps, A., Courboulex, F., Gaffet, S., Lomax, A., Virieux, J., Amato, A., Azzara, A., Castello, B., Chiarabba, C., & Cimini, G. (2000). Spatio-temporal distribution of seismic activity during the Umbria-Marche crisis, 1997. *Journal of Seismology*, *4*(4), 377-386.

Enescu, B., Mori, J., & Miyazawa, M. (2007). Quantifying early aftershock activity of the 2004 mid-Niigata Prefecture earthquake (Mw6.6). *Journal of Geophysical Research: Solid Earth*, *112*(B4). https://doi.org/10.1029/2006JB004629

Fielding, E. J., Liu, Z., Stephenson, O. L., Zhong, M., Liang, C., Moore, A., Yun, S., & Simons, M. (2020). Surface Deformation Related to the 2019 M w 7.1 and 6.4 Ridgecrest Earthquakes in California from GPS, SAR Interferometry, and SAR Pixel Offsets. *Seismological Research Letters*.

Gasperini, P., Lolli, B., & Vannucci, G. (2013). Empirical calibration of local magnitude data sets versus moment magnitude in Italy. *Bulletin of the Seismological Society of America*, *103*(4), 2227-2246.

Goebel, T. H. W., Schorlemmer, D., Becker, T. W., Dresen, G., & Sammis, C. G. (2013). Acoustic emissions document stress changes over many seismic cycles in stick-slip experiments. *Geophysical Research Letters*, *40*(10), 2049-2054. https://doi.org/10.1002/grl.50507

Gulia, L., Tormann, T., Wiemer, S., Herrmann, M., & Seif, S. (2016). Short-term probabilistic earthquake risk assessment considering time-dependent b values. *Geophysical Research Letters*, *43*(3), 1100-1108. https://doi.org/10.1002/2015GL066686

Gulia, L., & Wiemer, S. (2019). Real-time discrimination of earthquake foreshocks and aftershocks. *Nature*, *574*(7777), 193-199.

Gulia, L., Wiemer, S., & Vannucci, G. (2020). Pseudoprospective Evaluation of the Foreshock Traffic-Light System in Ridgecrest and Implications for Aftershock Hazard Assessment. *Seismological Society of America*, *91*(5), 2828-2842.

Guo, Z., & Ogata, Y. (1997). Statistical relations between the parameters of aftershocks in time, space, and magnitude. *Journal of Geophysical Research: Solid Earth*, *102*(B2), 2857-2873.

Gutenberg, G., & Richter, C. (1950). Seismicity of the earth and associated phenomena, Howard Tatel. *JGR*, *55*, 97.

Hauksson, E. (2015). Average Stress Drops of Southern California Earthquakes in the Context of Crustal Geophysics : Implications for Fault Zone Healing. *Pure and Applied Geophysics*, *172*(5), 1359-1370. https://doi.org/10.1007/s00024-014-0934-4

Hauksson, E., Hutton, K., Kanamori, H., Jones, L., Mori, J., Hough, S., & Roquemore, G. (1995). Preliminary Report on the 1995 Ridgecrest Earthquake Sequence in Eastern California. *Seismological Research Letters*, *66*(6), 54-60. https://doi.org/10.1785/gssrl.66.6.54

Hirakawa, E., & Barbour, A. J. (2020). Kinematic Rupture and 3D Wave Propagation Simulations of the 2019 Mw 7.1 Ridgecrest, California, Earthquake. *Bulletin of the Seismological Society of America*, *110*(4), 1644-1659. https://doi.org/10.1785/0120200031

Hudnut, K. W., Seeber, L., & Pacheco, J. (1989a). Cross-fault triggering in the November 1987 Superstition Hills earthquake sequence, southern California. *Geophysical Research Letters*, *16*(2), 199-202.

Kanamori, H. (1994). MECHANICS OF EARTHQUAKES. *Annual Review of Earth and Planetary Sciences*, *22*(1), 207-237. https://doi.org/10.1146/annurev.ea.22.050194.001231

Kariche, J. (2022). The 2020 Monte Cristo (Nevada) Earthquake Sequence : Stress Transfer in the Context of Conjugate Strike-Slip Faults. *Tectonics*, *41*(3), e2020TC006506.

Kariche, J., Meghraoui, M., Timoulali, Y., Cetin, E., & Toussaint, R. (2018). The Al Hoceima earthquake sequence of 1994, 2004 and 2016 : Stress transfer and poroelasticity in the Rif and Alboran Sea region. *Geophysical Journal International*, *212*(1), 42-53. https://doi.org/10.1093/gji/ggx385

Khoshmanesh, M., & Shirzaei, M. (2018). Episodic creep events on the San Andreas Fault caused by pore pressure variations. *Nature geoscience, 11*(8), 610.

Lozos, J. C., & Harris, R. A. (2020). Dynamic Rupture Simulations of the *M* 6.4 and *M* 7.1 July 2019 Ridgecrest, California, Earthquakes. *Geophysical Research Letters*, *47*(7). https://doi.org/10.1029/2019GL086020

Main, I. G., Meredith, P. G., Sammonds, P. R., & Jones, C. (1990). Influence of fractal flaw distributions on rock deformation in the brittle field. *Geological Society, London, Special Publications*, *54*(1), 81-96.

Malagnini, L., Lucente, F. P., De Gori, P., Akinci, A., & Munafo', I. (2012). Control of pore fluid pressure diffusion on fault failure mode : Insights from the 2009 L'Aquila seismic sequence. *Journal of Geophysical Research: Solid Earth*, *117*(B5).

Miller, S. A. (2020). Aftershocks are fluid-driven and decay rates controlled by permeability dynamics. *Nature communications*, *11*(1), 1-11.

Monastero, F. C., Walker, J. D., Katzenstein, A. M., Sabin, A. E., Glazner, A., & Bartley, J. (2002). Neogene evolution of the Indian Wells Valley, east-central California. *Geologic evolution of the Mojave Desert and southwestern Basin and Range: Geological Society of America Memoir*, *195*, 199-228.

Moro, M., Saroli, M., Stramondo, S., Bignami, C., Albano, M., Falcucci, E., Gori, S., Doglioni, C., Polcari, M., & Tallini, M. (2017). New insights into earthquake precursors from InSAR. *Scientific reports*, *7*(1), 12035.

Nanjo, K., Hirata, N., Obara, K., & Kasahara, K. (2012). Decade-scale decrease inb value prior to the M9-class 2011 Tohoku and 2004 Sumatra quakes. *Geophysical Research Letters*, *39*(20).

Nespoli, M., Belardinelli, M. E., Gualandi, A., Serpelloni, E., & Bonafede, M. (2018). Poroelasticity and Fluid Flow Modeling for the 2012 Emilia-Romagna Earthquakes : Hints from GPS and InSAR Data. *Geofluids*, *2018*.

Nur, A. (1972). Dilatancy, pore fluids, and premonitory variations of ts/tp travel times. *Bulletin of the Seismological society of America*, *62*(5), 1217-1222.

Nur, A., & Booker, J. R. (1972). Aftershocks caused by pore fluid flow? *Science*, *175*(4024), 885-887.

Ogata, Y., & Omi, T. (2020). Statistical Monitoring and Early Forecasting of the Earthquake Sequence : Case Studies after the 2019 M 6.4 Searles Valley Earthquake, California. *Bulletin of the Seismological Society of America*.

Pino, N. A., Convertito, V., & Madariaga, R. (2019). Clock advance and magnitude limitation through fault interaction : The case of the 2016 central Italy earthquake sequence. *Scientific reports*, *9*(1), 5005.

Pio Lucente, F., De Gori, P., Margheriti, L., Piccinini, D., Di Bona, M., Chiarabba, C., & Piana Agostinetti, N. (2010). Temporal variation of seismic velocity and anisotropy before the 2009 MW 6.3 L'Aquila earthquake, Italy. *Geology*, *38*(11), 1015-1018.

Proctor, B., Lockner, D., Kilgore, B., Mitchell, T., & Beeler, N. (2020). Direct evidence for fluid pressure, dilatancy, and compaction affecting slip in isolated faults. *Geophysical Research Letters*, *47*(16), e2019GL086767.

Rice, J. R. (1992). Chapter 20 Fault Stress States, Pore Pressure Distributions, and the Weakness of the San Andreas Fault. In *International Geophysics* (Vol. 51, p. 475-503). Elsevier. https://doi.org/10.1016/S0074-6142(08)62835-1

Rikitake, T. (1972). Earthquake prediction studies in Japan. *Geophysical surveys*, *1*(1), 4-26.

Ross, Z. E., Trugman, D. T., Hauksson, E., & Shearer, P. M. (2019). Searching for hidden earthquakes in Southern California. *Science*, *364*(6442), 767-771.

Ruhl, C., Abercrombie, R., Smith, K., & Zaliapin, I. (2016). Complex spatiotemporal evolution of the 2008 Mw 4.9 Mogul earthquake swarm (Reno, Nevada) : Interplay of fluid and faulting. *Journal of Geophysical Research: Solid Earth*, *121*(11), 8196-8216.

Sammonds, P., Meredith, P., & Main, I. (1992). Role of pore fluids in the generation of seismic precursors to shear fracture. *Nature*, *359*(6392), 228-230.

Scholz, C. H. (1968). The frequency-magnitude relation of microfracturing in rock and its relation to earthquakes. *Bulletin of the Seismological Society of America*, *58*(1), 399-415. https://doi.org/10.1785/BSSA0580010399

Scholz, C. H. (2015). On the stress dependence of the earthquake b value. *Geophysical Research Letters*, *42*(5), 1399-1402.

Scholz, C. H. (2019). *The mechanics of earthquakes and faulting*. Cambridge university press.

Scholz, C. H., Sykes, L. R., & Aggarwal, Y. P. (1973). Earthquake prediction : A physical basis. *Science*, *181*(4102), 803-810.

Scholz, C., & Kranz, R. (1974). Notes on dilatancy recovery. *Journal of Geophysical Research*, *79*(14), 2132-2135.

Segall, P., & Rice, J. R. (1995). Dilatancy, compaction, and slip instability of a fluid-infiltrated fault. *Journal of Geophysical Research: Solid Earth*, *100*(B11), 22155-22171.

Shearer, P. M., Prieto, G. A., & Hauksson, E. (2006). Comprehensive analysis of earthquake source spectra in southern California : SOUTHERN CALIFORNIA SOURCE SPECTRA. *Journal of Geophysical Research: Solid Earth*, *111*(B6), n/a-n/a. https://doi.org/10.1029/2005JB003979

Shelly, D. R. (2020). A high-resolution seismic catalog for the initial 2019 Ridgecrest earthquake sequence : Foreshocks, aftershocks, and faulting complexity. *Seismological Research Letters*.

Sheng, S., & Meng, L. (2020). Stress Field Variation During the 2019 Ridgecrest Earthquake Sequence. *Geophysical Research Letters*, *47*(15), e2020GL087722.

Shi, Y., & Bolt, B. A. (1982). The standard error of the magnitude-frequency b value. *Bulletin of the Seismological Society of America*, *72*(5), 1677-1687.

Smith, W. D. (1981). The b-value as an earthquake precursor. *Nature*, *289*(5794), 136-139.

Soldati, G., Zaccarelli, L., & Faenza, L. (2019). Spatio-temporal seismic velocity variations associated to the 2016–2017 central Italy seismic sequence from noise cross-correlation. *Geophysical Journal International*, *219*(3), 2165-2173.

Stramondo, S., Tesauro, M., Briole, P., Sansosti, E., Salvi, S., Lanari, R., Anzidei, M., Baldi, P., Fornaro, G., & Avallone, A. (1999). The September 26, 1997 Colfiorito, Italy, earthquakes : Modeled coseismic surface displacement from SAR interferometry and GPS. *Geophysical research letters*, *26*(7), 883-886.

Tan, Y. J., Waldhauser, F., Ellsworth, W. L., Zhang, M., Zhu, W., Michele, M., Chiaraluce, L., Beroza, G. C., & Segou, M. (2021). Machine-learning-based high-resolution earthquake catalog reveals how complex fault structures were activated during the 2016–2017 Central Italy sequence. *The Seismic Record*, *1*(1), 11-19.

Tong, P., Yao, J., Liu, Q., Li, T., Wang, K., Liu, S., Cheng, Y., & Wu, S. (2021). Crustal rotation and fluids : Factors for the 2019 Ridgecrest earthquake sequence? *Geophysical Research Letters*, *48*(3), e2020GL090853.

Tormann, T., Wiemer, S., Metzger, S., Michael, A., & Hardebeck, J. L. (2013). Size distribution of Parkfield's microearthquakes reflects changes in surface creep rate. *Geophysical Journal International*, *193*(3), 1474-1478. https://doi.org/10.1093/gji/ggt093

Trugman, D. T. (2020). Stress-Drop and Source Scaling of the 2019 Ridgecrest, California, Earthquake Sequence. *Bulletin of the Seismological Society of America*.

Utsu, T., & Ogata, Y. (1995). The centenary of the Omori formula for a decay law of aftershock activity. *Journal of Physics of the Earth*, *43*(1), 1-33.

Wang, K., & Bürgmann, R. (2020). Co- and Early Postseismic Deformation Due to the 2019 Ridgecrest Earthquake Sequence Constrained by Sentinel-1 and COSMO-SkyMed SAR Data. *Seismological Research Letters*. https://doi.org/10.1785/0220190299

Wiemer, S. (2001). A software package to analyze seismicity : ZMAP. *Seismological Research Letters*, *72*(3), 373-382.

Wiemer, S., & Wyss, M. (2000). Minimum magnitude of completeness in earthquake catalogs : Examples from Alaska, the western United States, and Japan. *Bulletin of the Seismological Society of America*, *90*(4), 859-869.

Woessner, J., & Wiemer, S. (2005). Assessing the quality of earthquake catalogues : Estimating the magnitude of completeness and its uncertainty. *Bulletin of the Seismological Society of America*, *95*(2), 684-698.

Wyss, M., & Habermann, R. E. (1988). Precursory seismic quiescence. *Pure and Applied Geophysics*, *126*(2), 319-332.

Wyss, M., & McNutt, S. R. (1998). Temporal and three-dimensional spatial analyses of the frequency–magnitude distribution near Long Valley Caldera, California. *Geophysical Journal International*, *134*(2), 409-421.

Wyss, M., & Wiemer, S. (2000). Change in the probability for earthquakes in southern California due to the Landers magnitude 7.3 earthquake. *Science*, *290*(5495), 1334-1338.

Xu, X., Sandwell, D. T., & Smith-Konter, B. (2020). Coseismic Displacements and Surface Fractures from Sentinel-1 InSAR : 2019 Ridgecrest Earthquakes. *Seismological Research Letters*. https://doi.org/10.1785/0220190275

Supplemental Material

Role of fluid on earthquake occurrence: Example of the 2019 Ridgecrest and the 1997-2016 Central Apennines sequences

by J.Kariche

List of Figure Captions

Figure S1

Seismotectonic map of the southern Walker Lane including the 1872 Owens Valley earthquake and its major aftershocks. The 1872 Owens Valley focal mechanism solutions and locations are from Deng & Sykes. (1997). The fault ruptures trace associated with the 1872 Owens Valley earthquake is represented by thick lines. The focal solutions of the Mw 6.4 and Mw 7.1 Ridgecrest earthquakes are from USGS-NEIC. The fault trace related to the 2019 Ridgecrest sequence (thick lines) is from Ross et al. (2019). The Quaternary active faults associated with the Walker Lane domain and ECSZ are from the USGS database (https://earthquake.usgs.gov/hazards/qfaults/, last updated in 2017).

Figure S2

Seismicity analysis along the central Apennines spanning the period from 1985 to 01/01/2009

A) Map of seismicity centered on the 1997 Colfiorito earthquake sequences. The yellow stars represent the location of major events with Mw>5.0. The blue lines represent the location of major actives faults in central Italy obtained from the EDSF project (Basili et al., 2013). The green lines represent the surface projection of the Colfiori faults plane (based on the rupture model of Hernandez et al.(2004). The purple lines represent the updated actives faults for

Central Apennines extracted from the Fault2SHA project (Scotti et al., 2021). **B)** Depth through time cross-section for a period between 1985 to pre-L'Aquila mainshock.

C) Cross-section along rectangular volume (in red in Figure S1A) oriented NW-SE. The yellows stars are major earthquakes related to the 1997 Colfiorito sequence as shown in the paper (figure 1). Note that the selected events for Cross-section in B) and C) are the earthquakes inside the Cross-section CC'.

Figure S3

Seismicity analysis along the central Apennines covering the period from 01/01/2009 to 01/05/2009.

A) Map of seismic events related to the 06/04/2009 (Mw 6.3) L'Aquila sequence. The black rectangles represent plotted seismicity start on January 1, 2009 and finish just before the Mw6.3 L'Aquila mainshocks. The grey rectangles represent the aftershocks activity following the Mw6.3 2009 L'Aquila earthquake and cut on June14, 2009. The yellow stars represent the location of the L'Aquila mainshock. **B)** Frequency Magnitude Distribution FMD in the ~ 3 months before the L'Aquila earthquake. The b and Mc values are obtained by a maximum curvature estimate (Wiemer & Wyss, 2000). **C)** Time–depth cross-section of ~3-month seismicity before the L'Aquila mainshock.

Figure S4

Seismicity analysis following the 2016 (Mw6.5) Norcia sequence.

A) Aftershock distribution related to the Mw6.5 30/10/2016 Norcia earthquake. The yellow star represents the location of the mainshock, the grey star represents the location of the 24/08/2016 Amatrice Foreshock. **B)** Cumulative events time series in the Norcia basin spanning the period from 1985 to 2017. **C)** FMD associated with the 2016 Norcia earthquake sequence, uncertainties are obtained by maximum curvature estimate (Wiemer & Wyss, 2000).

Figure S5

Seismicity analysis in Southern California.

A) Spatial distribution of seismicity in ECSZ spanning the period from 2000 to 2019. **B)** Cumulative earthquakes time series plot in ECSZ from periods range from 2000 to 2019, the yellow stars represent the time location of the Mw6.4 Foreshock and the Mw7.1 mainshock. **C)** FMD for the 2019 Ridgecrest earthquake sequence. The Magnitude of completeness is obtained using the maximum likelihood approach. The G-R values (a and b) are obtained using the maximum curvature estimate. The earthquake catalog using for this supplemental material is the same as in the main article.

Figure S6

Time evolution of the number of earthquakes from 2000 to August 2019 associated to a seismogenic volume around the Ridgecrest fault zone through each point of the b-value time series. The b-value time series was performed using time windows with selected earthquakes with radius R~ 30 km centered at coordinate = (-117,7243°, 35.7031°). The calculation method is based on the Maximum curvature approach with sample windows size = 250 events and windows overlap of 4%.

Figure S7

Time evolution of the number of earthquakes from 2007 to August 2017 associated to the central Appennines fault zone through each point of the b-value time series. The calculation method is the same as in the Figure S6.

Figure S8

Comparison of b-value time-series for various constant number of event N associated to the 2016 Amatrice earthquake sequence. The sampling technique is based on using a moving windows approach of a fixed number of N events. This approach gives a robust estimate from different lengths of time windows. The b-value time series show that the shape of time series is preserved for $100 \leq N \leq 500$.

Figure S9

Comparison of b-value time-series for various constant number of event N associated to the 2019 Ridgecrest earthquake sequence. The sampling technique is the same as in figure S9. As for the Amatrice case, the b-value time series show that the shape of time series is preserved for $100 \leq N \leq 500$.

Figure S10

Geographical footprint related to the selected earthquake (datasets on the polygon) and used to construct Figure 7 of the manuscript. As for Figure 7, the catalog used here is defined as the combination of the INGV and the Gasperini et al. (2013) catalogs. For all Figures, the seismicity analysis is made using the Zmap 7 software (Reyes & Wiemer, 2020).

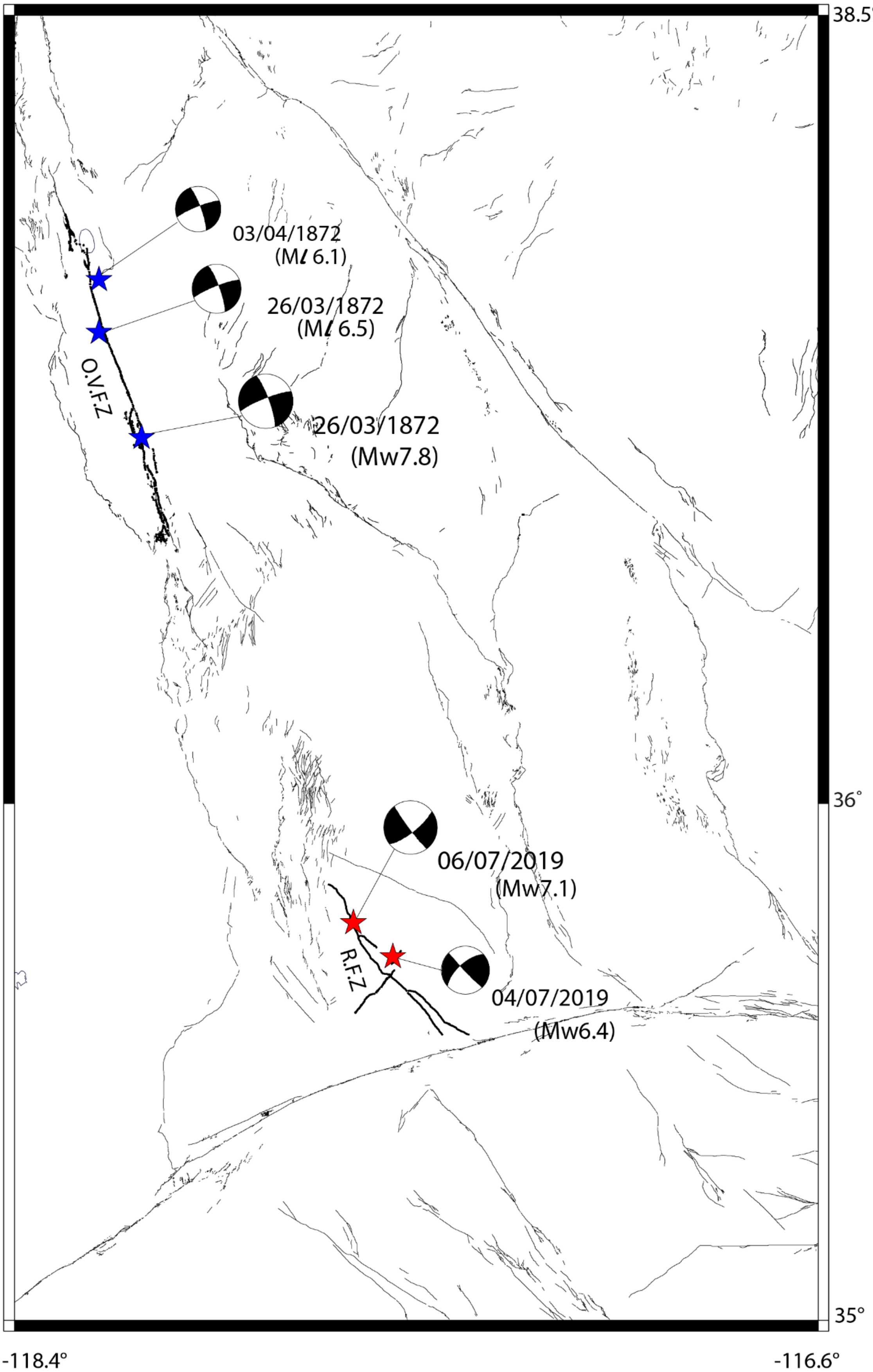

38.5°
03/04/1872
(Ml 6.1)
26/03/1872
(Ml 6.5)
O.V.F.Z
26/03/1872
(Mw7.8)
36°
06/07/2019
(Mw7.1)
R.F.Z
04/07/2019
(Mw6.4)
35°
-118.4°
-116.6°

Figure S1

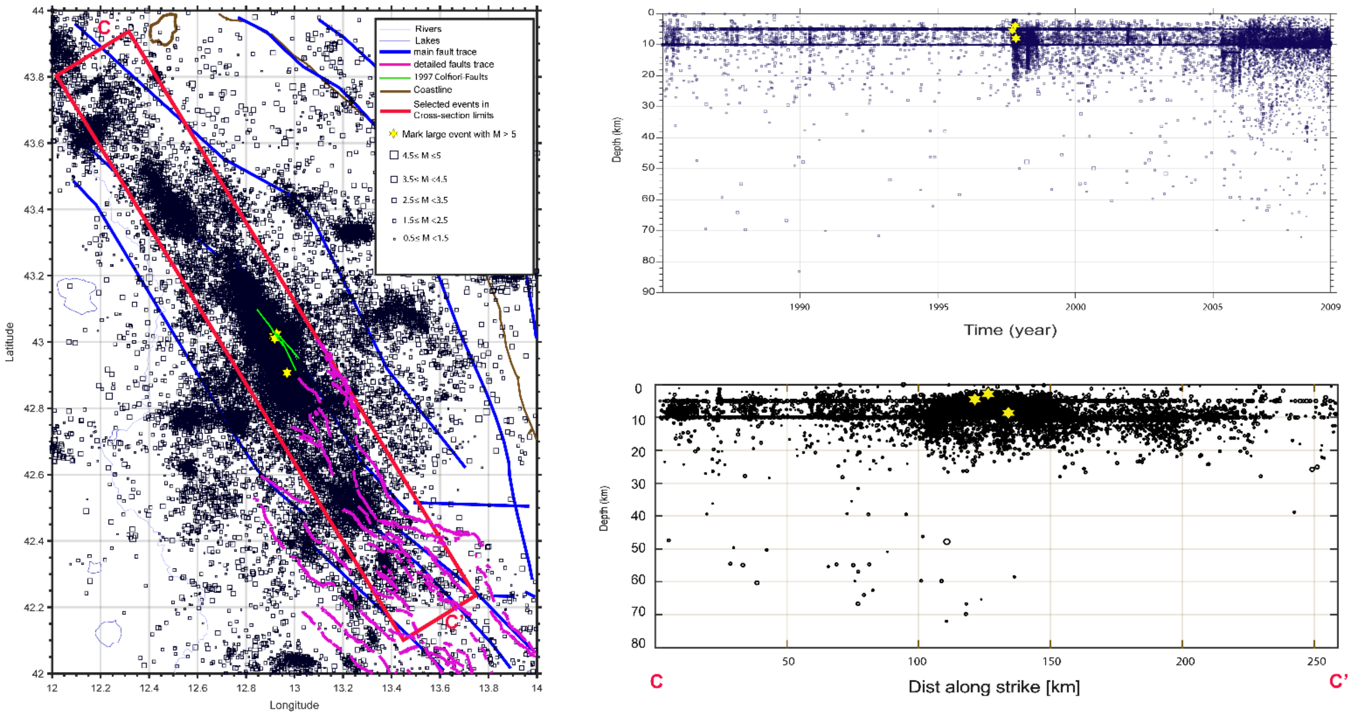

Figure S2

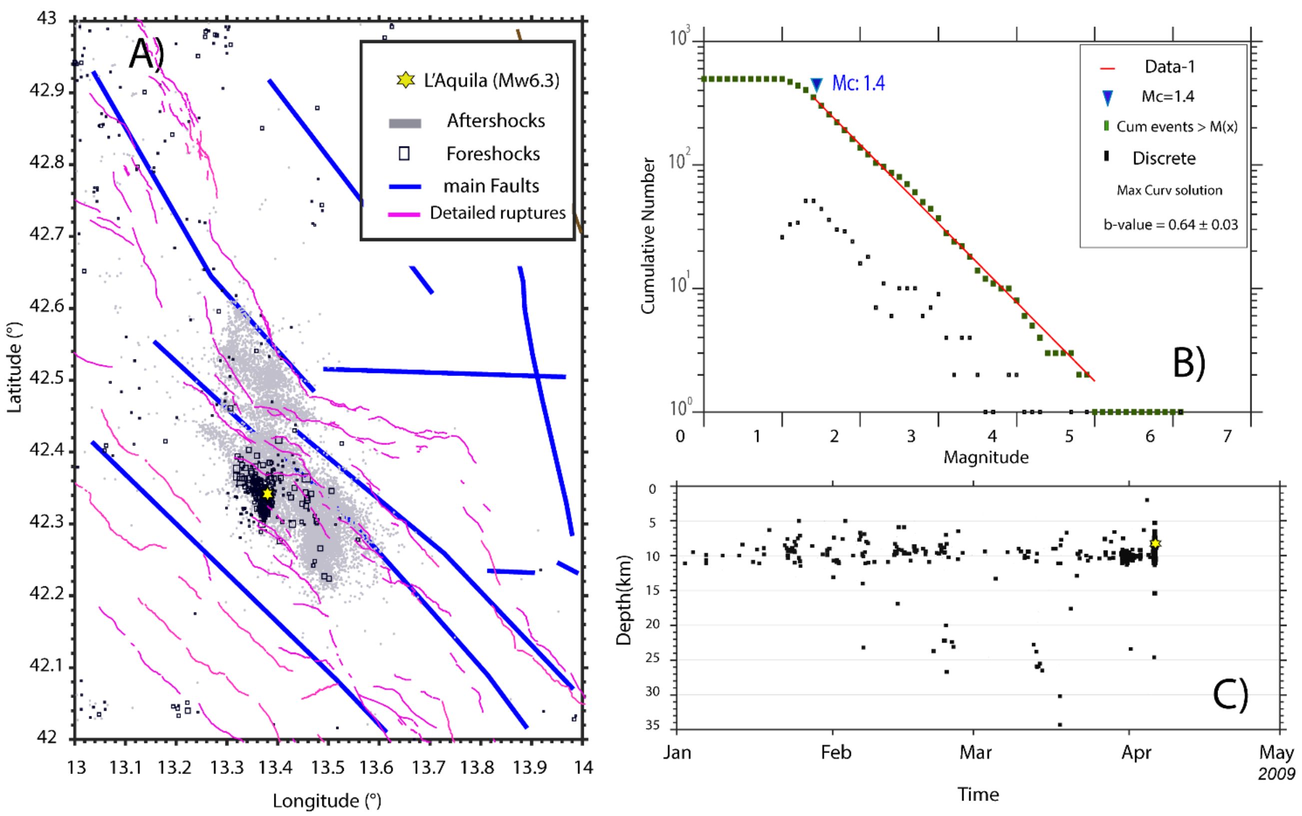

Figure S3

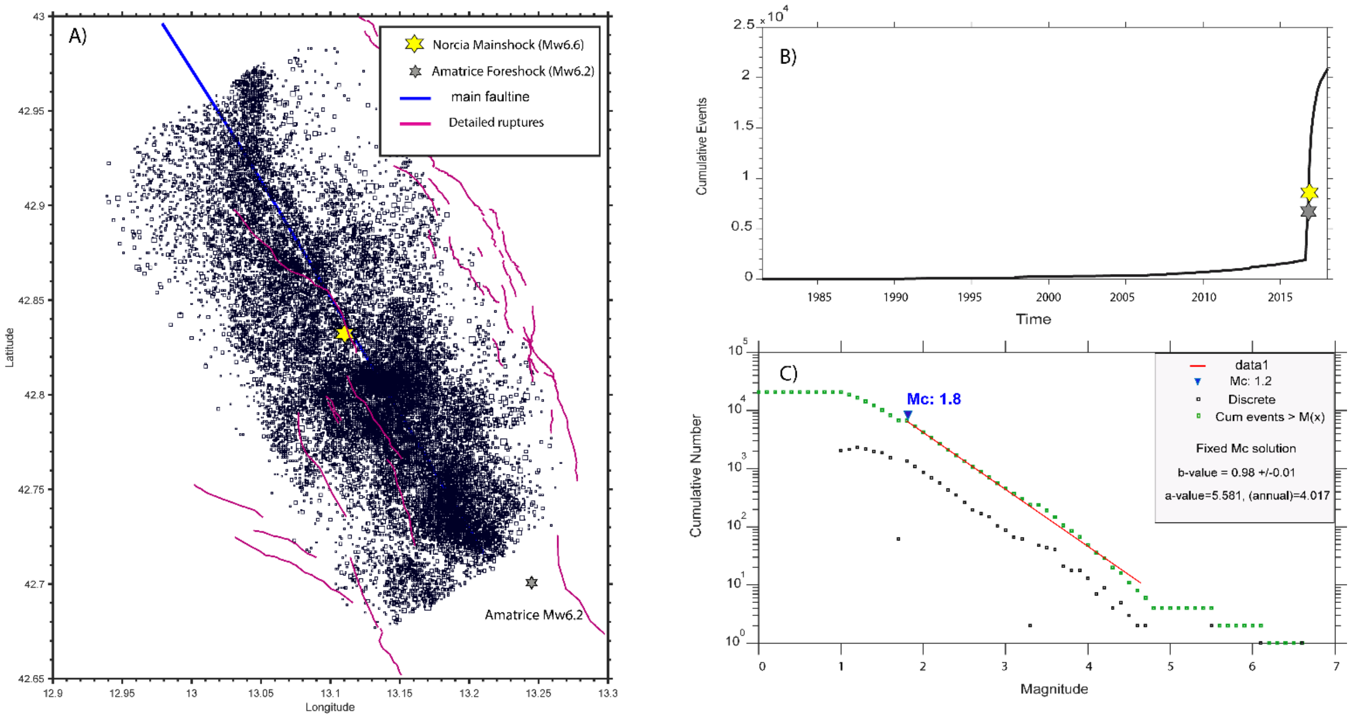

Figure S4

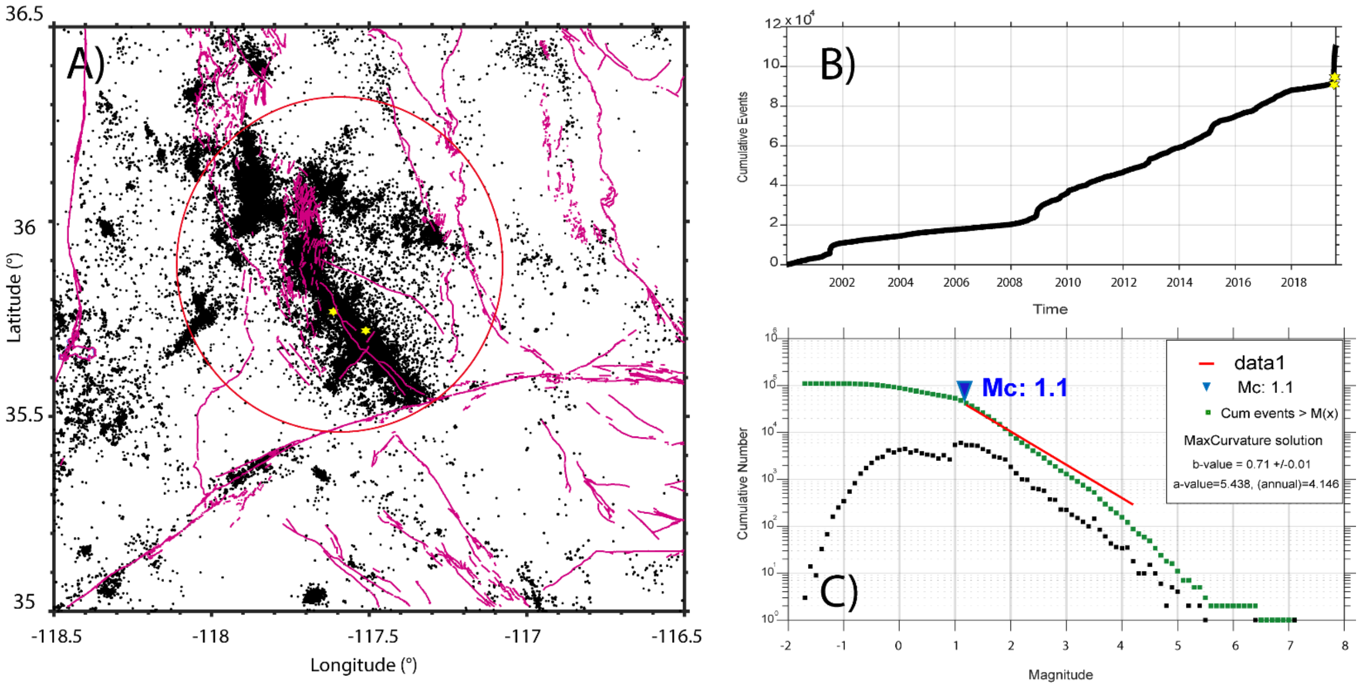

Figure S5

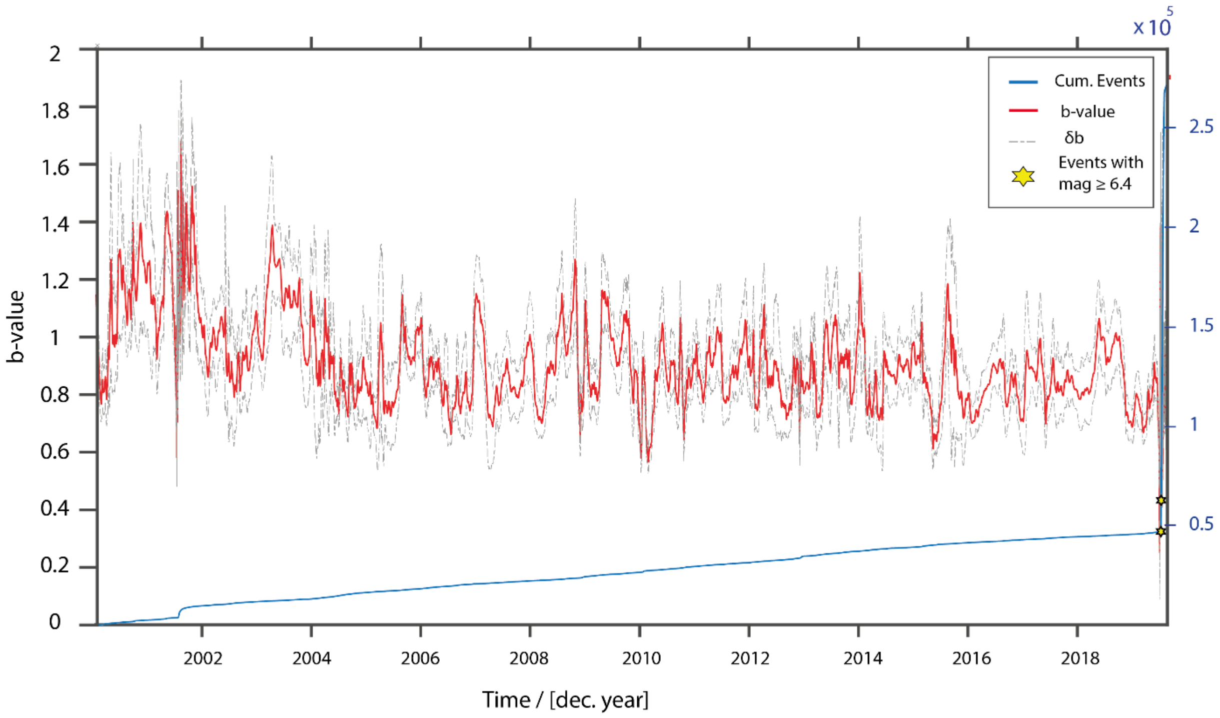

Figure S6

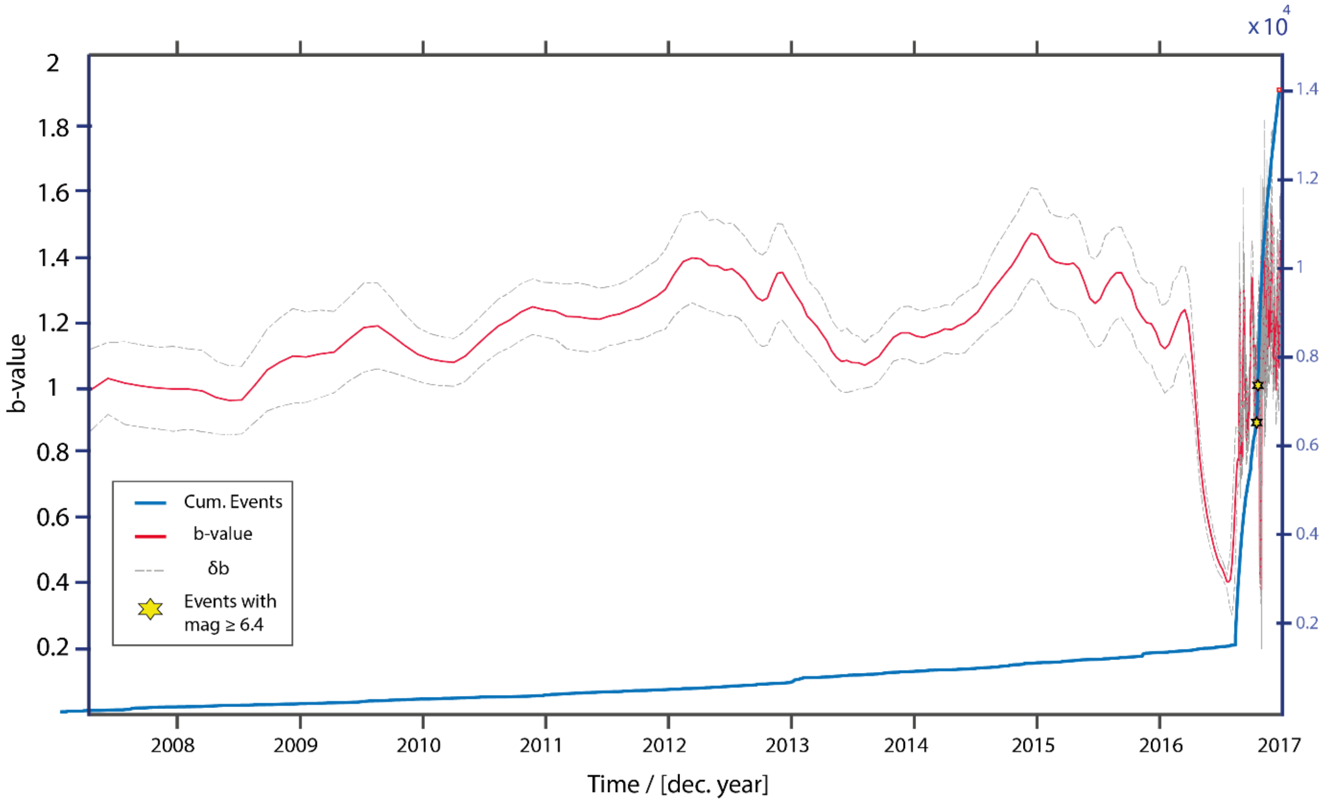

Figure S7

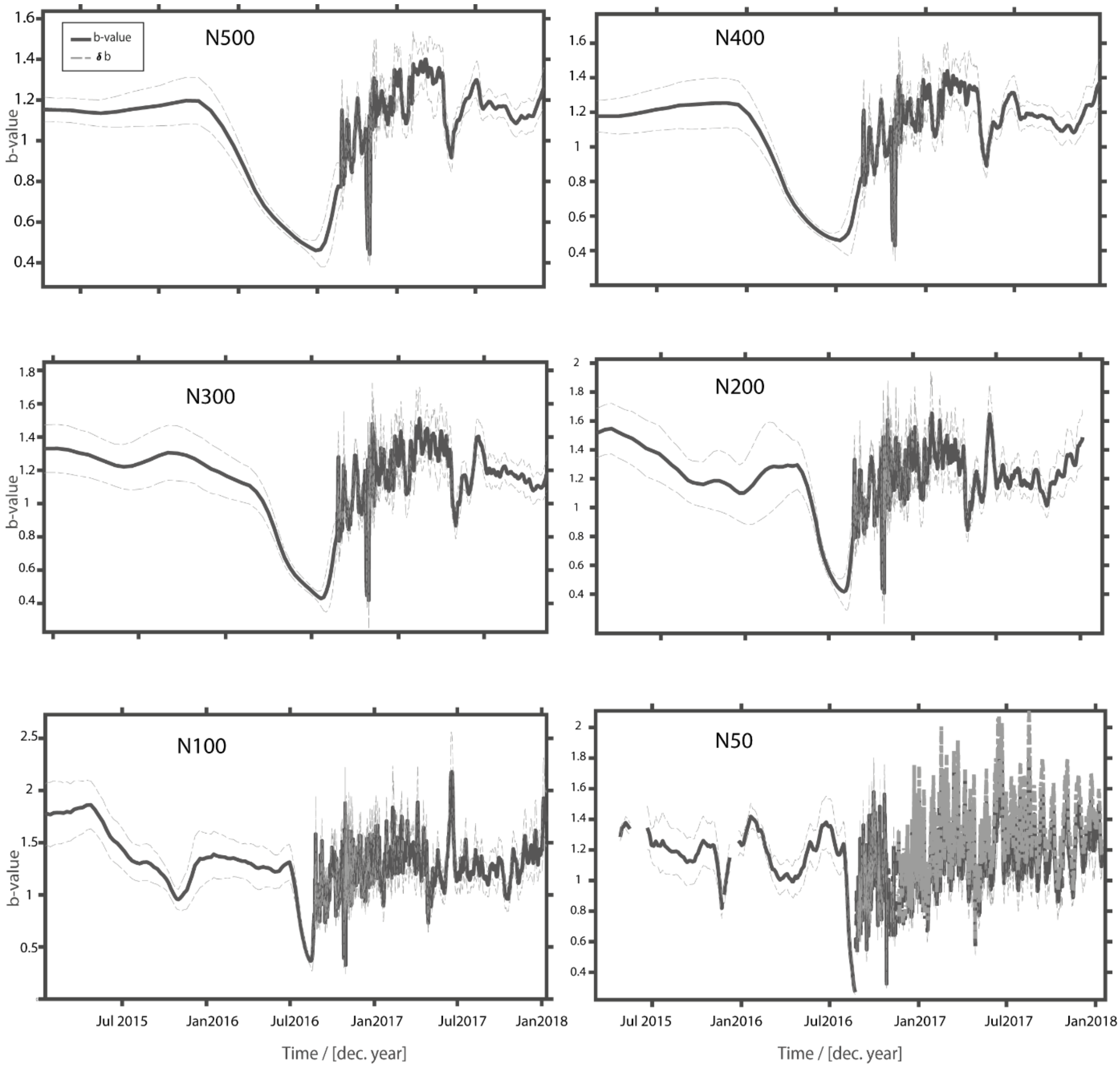

N500
b-value
δ b
N400
N300
N200
N100
N50
b-value
Jul 2015
Jan2016
Jul2016
Jan2017
Jul2017
Jan2018
Time / [dec. year]

Figure S8

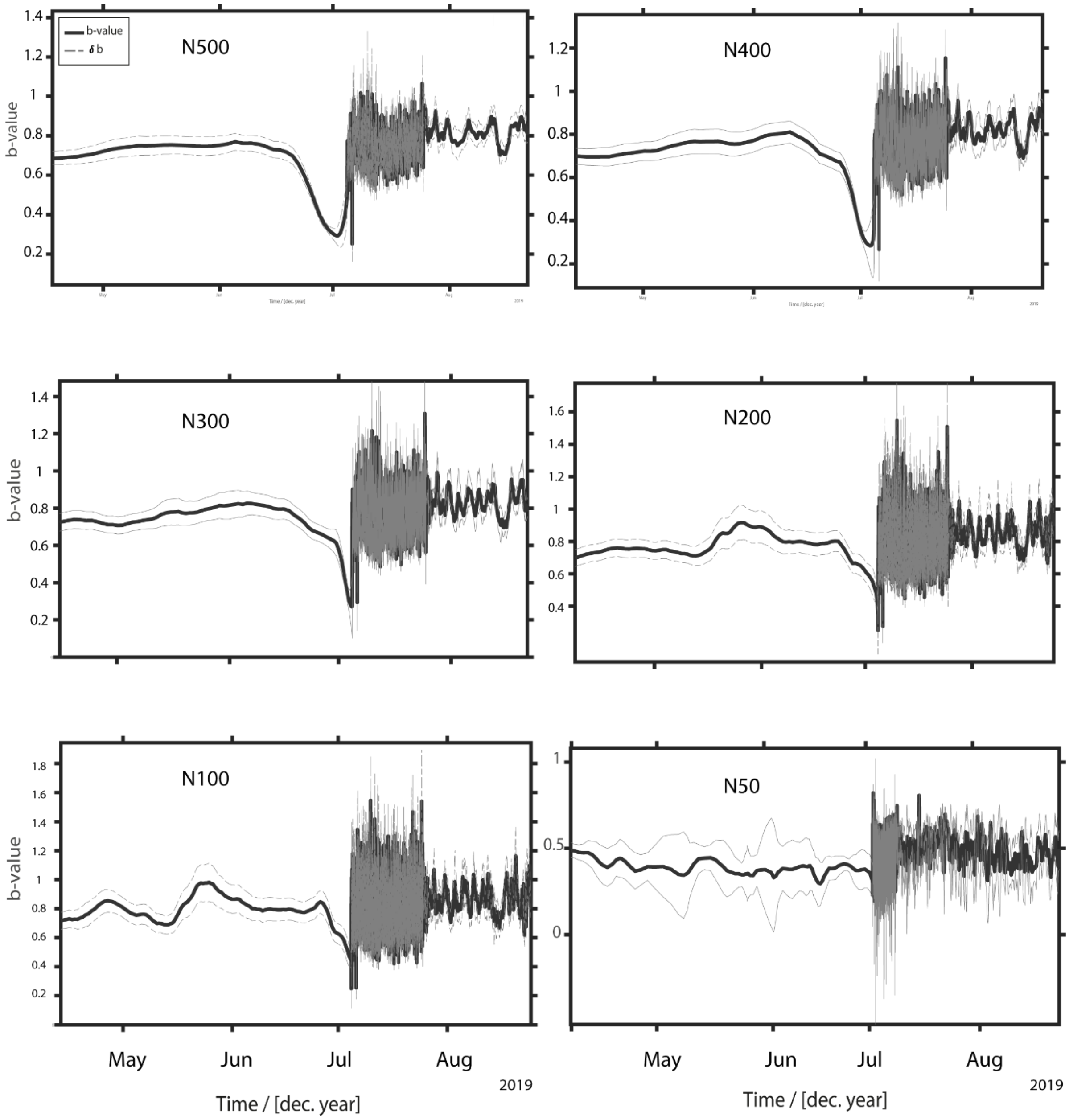
N500
N400
N300
N200
N100
N50
b-value
δb
May
Jun
Jul
Aug
2019
Time / [dec. year]

Figure S9

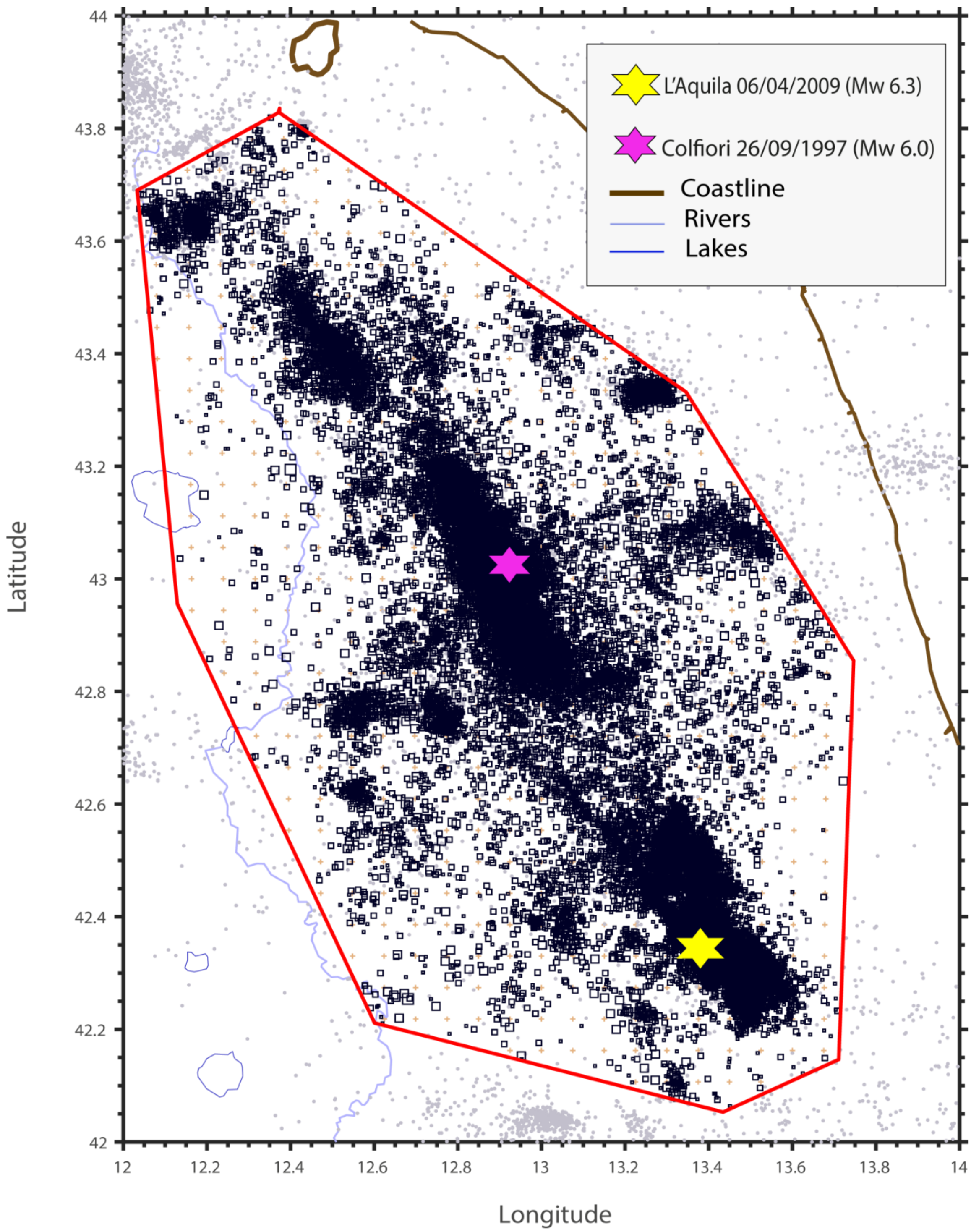

L'Aquila 06/04/2009 (Mw 6.3)
Colfiori 26/09/1997 (Mw 6.0)
Coastline
Rivers
Lakes
Latitude
Longitude
44
43.8
43.6
43.4
43.2
43
42.8
42.6
42.4
42.2
42
12
12.2
12.4
12.6
12.8
13
13.2
13.4
13.6
13.8
14

Figure S10

References

Basili, R., Kastelic, V., Demircioglu, M. B., Garcia Moreno, D., Nemser, E. S., Petricca, P., Sboras, S. P., Besana-Ostman, G. M., Cabral, J., Camelbeeck, T., Caputo, R., Danciu, L., Domaç, H., Fonseca, J. F. de B. D., García-Mayordomo, J., Giardini, D., Glavatovic, B., Gulen, L., Ince, Y., … Wössner, J. (2013). *European Database of Seismogenic Faults (EDSF)* (p. 1131 fault sources) [Text/html,application/vnd.google-earth.kml+xml,application/vnd.mif,application/x-zipped-shp]. Istituto Nazionale di Geofisica e Vulcanologia (INGV). https://doi.org/10.6092/INGV.IT-SHARE-EDSF

Deng, J., & Sykes, L. R. (1997). Evolution of the stress field in southern California and triggering of moderate-size earthquakes: A 200-year perspective. *Journal of Geophysical Research: Solid Earth*, *102*(B5), 9859-9886.

Gasperini, P., Lolli, B., & Vannucci, G. (2013). Empirical calibration of local magnitude data sets versus moment magnitude in Italy. *Bulletin of the Seismological Society of America*, *103*(4), 2227-2246.

Hernandez, B., Cocco, M., Cotton, F., Stramondo, S., Scotti, O., Courboulex, F., & Campillo, M. (2004). Rupture history of the 1997 Umbria-Marche (Central Italy) main shocks from the inversion of GPS, DInSAR and near field strong motion data. *Annals of Geophysics*, *47*(4).

Reyes, C., & Wiemer, S. (2020). *From ZMAP to ZMAP7 : Fast-forwarding 25 years of software evolution*. 18878.

Ross, Z. E., Idini, B., Jia, Z., Stephenson, O. L., Zhong, M., Wang, X., Zhan, Z., Simons, M., Fielding, E. J., & Yun, S.-H. (2019). Hierarchical interlocked orthogonal faulting in the 2019 Ridgecrest earthquake sequence. *Science*, *366*(6463), 346-351.

Scotti, O., Visini, F., Faure Walker, J., Peruzza, L., Pace, B., Benedetti, L., Boncio, P., & Roberts, G. (2021). Which fault threatens me most ? Bridging the gap between geologic data-providers and seismic risk practitioners. *Frontiers in Earth Science, 8*, 626401.

Wiemer, S., & Wyss, M. (2000). Minimum magnitude of completeness in earthquake catalogs : Examples from Alaska, the western United States, and Japan. *Bulletin of the Seismological Society of America, 90*(4), 859-869.